

MatchAttention: Matching the Relative Positions for High-Resolution Cross-View Matching

Tingman Yan[✉], Tao Liu[✉], *Senior Member, IEEE*, Xilian Yang[✉], Qunfei Zhao[✉],
Zeyang Xia[✉], *Senior Member, IEEE*

Abstract—Cross-view matching is fundamentally achieved through cross-attention mechanisms. However, matching of high-resolution images remains challenging due to the quadratic complexity and lack of explicit matching constraints in the existing cross-attention. This paper proposes an attention mechanism, MatchAttention, that dynamically matches relative positions. The relative position determines the attention sampling center of the key-value pairs given a query. Continuous and differentiable sliding-window attention sampling is achieved by the proposed BilinearSoftmax. The relative positions are iteratively updated through residual connections across layers by embedding them into the feature channels. Since the relative position is exactly the learning target for cross-view matching, an efficient hierarchical cross-view decoder, MatchDecoder, is designed with MatchAttention as its core component. To handle cross-view occlusions, gated cross-MatchAttention and a consistency-constrained loss are proposed. These two components collectively mitigate the impact of occlusions in both forward and backward passes, allowing the model to focus more on learning matching relationships. When applied to stereo matching, MatchStereo-B ranked 1st in average error on the public Middlebury benchmark and requires only 29ms for KITTI-resolution inference. MatchStereo-T can process 4K UHD images in 0.1 seconds using only 3GB of GPU memory. The proposed models also achieve state-of-the-art performance on KITTI 2012, KITTI 2015, ETH3D, and Spring flow datasets. The combination of high accuracy and low computational complexity makes real-time, high-resolution, and high-accuracy cross-view matching possible. Project page: <https://tingmanyan.github.io/MatchAttention/>.

Index Terms—Attention mechanism, Relative Position, Cross-view matching, Stereo matching, Optical flow.

1 INTRODUCTION

CROSS-view matching is a fundamental component of 3D vision, enabling cross-view correspondence under geometric constraints: In stereo matching, it determines dense correspondences constrained by epipolar geometry for disparity calculation; in optical flow, it tracks temporal pixel displacements between sequential frames to estimate motion fields; while in feature matching, it extracts sparse yet discriminative correspondences that serve as anchors for camera pose optimization. Recent advancements in 3D reconstruction frameworks, exemplified by DUST3R [1], highlight the effectiveness of cross-view matching in achieving geometry-consistent 3D point map estimation. Moreover, state-of-the-art (SOTA) feed-forward 3D Gaussian splatting methods [2], [3], [4] utilize cross-view matching to extract geometric information across multiple views, enabling precise predictions of 3D Gaussian parameters. The widespread use of cross-view matching across various 3D vision tasks underscores its critical role in fostering accurate 3D representations and enhancing spatial intelligence capabilities.

Cross-view matching can be implemented using convolutional or transformer architectures. For convolutional architectures, the matching relationship is established through a cost volume that captures feature similarities between reference and target views. However, for general cross-view

matching tasks without epipolar constraints as in stereo matching, the size of the cost volume grows proportionally to $(H \times W)^2$, thereby limiting the scalability of cost-volume-based methods to high resolutions. For transformer architectures, cross-view matching can be achieved through cross-attention with query tokens from the reference view and key, value tokens from the target view. UniMatch [5] leverages interleaved self- and cross-attention as a cross-view feature decoder for unified stereo matching and optical flow. The final features are correlated into a 3D/4D cost volume to regress disparity or flow. The global cross-attention mechanism has been widely adopted by various frameworks, including DUST3R [1], MAST3R [6], and feed-forward Gaussian splatting methods such as Splatt3R [3] and No-PoSplat [4]. However, the global cross-attention mechanism has quadratic complexity, which limits its scalability to high resolution. Furthermore, while it excels at aggregating cross-view features, it does not inherently enforce explicit matching constraints. To address this, additional correlation between aggregated features is often required for tasks that demand precise matching results [5], [6], [7].

In summary, the global cross-attention mechanism has two main disadvantages for cross-view matching: (1) quadratic complexity and (2) the lack of explicit matching. The latter can be explained by the fact that different query tokens from the reference view share the same matching tokens (all tokens) from the target view, which limits the ability to distinguish the matching relationship. To address these limitations of the global cross-attention and achieve high-resolution cross-view matching, an effective cross-attention mechanism should possess three essential

- Tingman Yan, Tao Liu, and Xilian Yang are with the Department of Automation, Dalian University of Technology, Dalian, 116024, China. E-mail: tingmanyan@dlut.edu.cn, tliu@dlut.edu.cn, yangxl@dlut.edu.cn
- Qunfei Zhao is with the Department of Automation, Shanghai Jiao Tong University, Shanghai, 200240, China. E-mail: zhaoqf@sjtu.edu.cn
- Zeyang Xia is with the School of Mechanical Engineering, Shanghai Jiao Tong University, Shanghai, 200240, China. E-mail: zxia@sjtu.edu.cn

properties: (1) long-range connections for large disparities, optical flow, and displacement matching; (2) explicit similarity and matching between queries and keys; and (3) linear complexity to support high-resolution inference.

For cross-view matching, **the relative position exactly represents the matching relation**, which is disparity for stereo matching and flow for optical flow. We propose MatchAttention, an attention mechanism that matches relative positions to address the above limitations of the global cross-attention. MatchAttention is a variant of sliding-window attention with *dynamic* and *contiguous* sampling positions relative to the given queries. The relative position R_{pos} is defined as the position difference between the sampling window center of key-value pairs and the query, where $R_{pos} \in \mathbb{R}^{H \times W \times 2}$. As shown in Figure 1, the token features and the relative position are concatenated and fed as input to MatchAttention. The relative position is learned and updated through the residual connection [8] and the matching relation within MatchAttention. Since the relative position is arbitrary, MatchAttention can achieve long-range connections, i.e., it can match any pair of tokens between the reference and the target views. The computational complexity is proportional to the sliding-window size and the number of tokens, resulting in linear complexity. Compared to global attention, MatchAttention samples a contiguous sub-window of tokens and concatenates the relative position with the features as input, while the rest remains consistent. MatchAttention computes the similarity of queries and keys with softmax activation and aggregates value tokens by the attention weights. Therefore, MatchAttention possesses the aforementioned three properties and can address the limitations of global cross-attention for high-resolution cross-view matching.

Attending to a subset of tokens or applying attention sampling has been explored in pioneering work [9], which is referred to as hard attention. Hard attention is non-differentiable because it samples discrete window locations. The local-predictive attention proposed in [10] addresses this limitation by predicting the sampling window’s aligned position using hidden states and softening the attention weights with a Gaussian kernel centered at the predicted position. However, as noted in their paper, local-predictive attention remains non-differentiable at certain points because the backward gradient of the predicted position is propagated through the Gaussian kernel rather than through the discrete sampling process itself. Deformable attention [11] for object detection attends to a small set of sampling tokens by predicting offsets and pre-softmax weights using the query features, which is differentiable and has linear complexity. However, both local-predictive attention and deformable attention predict sampling positions based solely on query features from a single view, neglecting cross-view matching information. We step further by considering the relationship between relative position and attention sampling and propose *BilinearSoftmax* for continuous and differentiable attention sampling. The sampling center (i.e., the key position) is determined by adding the relative position to the query position. Bilinear sampling is performed at the window level to reduce computational cost through window overlapping. In contrast, deformable attention samples at the pixel level, which requires $4 \times$ com-

plexity. The backward gradients of the relative positions are propagated via residual connections and the differentiable BilinearSoftmax.

We demonstrate the cross-view matching ability of MatchAttention on stereo matching and optical flow tasks. A hierarchical cross-view decoder (MatchDecoder) with interleaved self- and cross-MatchAttention modules is proposed. Since the matching relationship is intrinsically sparse, we introduce negative L1-norm as the attention similarity measure, which can be interpreted as a normalized Laplace kernel when combined with softmax. By inspecting the relative positions in self-MatchAttention, the sampling window positions of occluded regions can be visualized, achieving explainable occlusion handling. Through cross-view matching and feature aggregation, MatchDecoder enables accurate disparity/flow estimation for both views under supervision from the reference view only. We further propose four components to improve MatchDecoder. (1) Attention weights as local cost volume are injected to the projection layer to improve matching discriminability. (2) Unreliable cross-view aggregated features are filtered out by a gated mechanism to handle occlusion in the forward pass. (3) A consistency-constrained loss is employed for supervision to handle occlusion in the backward pass. (4) A running non-occlusion mask is embedded as an extra feature channel for occlusion awareness in self-MatchAttention. For high-resolution stereo matching and optical flow, MatchStereo-T can process 4K UHD stereo/flow image pairs in 0.1s with less than 3GB memory on an RTX 5090 GPU. Experiments demonstrate that MatchStereo-B achieves superior zero-shot generalization to all comparison methods on the real-world Middlebury [12] and ETH3D [13] datasets when trained only on synthetic Scene Flow datasets [14]. Notably, it requires only 1/8 and 1/30 of the computational cost (FLOPs) of RAFT-Stereo [15] and FoundationStereo [16], respectively.

In summary, our main contributions are as follows:

- We propose MatchAttention that attends to contiguous and dynamic sub-window tokens with window center determined by relative position. MatchAttention enables arbitrary relative position, explicit matching between queries and keys, and has linear complexity. The relative position is learned by residual connection and matching relation, and no additional positional embedding is required.
- We propose a hierarchical transformer decoder (MatchDecoder) with interleaved self- and cross-MatchAttention to demonstrate MatchAttention’s effectiveness for cross-view matching. Negative L1-norm as a similarity measure is also proposed in combination with MatchAttention to exploit the sparsity nature of matching.
- Gated cross-MatchAttention and consistency-constrained loss are proposed to filter out the interference of occlusion in both the forward and backward passes such that the network can focus on the learning of matching relation.
- MatchStereo-B ranked 1st on the Middlebury benchmark in terms of average error and also achieved state-of-the-art performance on KITTI 2012 Reflective [17], KITTI 2015 [18], and ETH3D [13] bench-

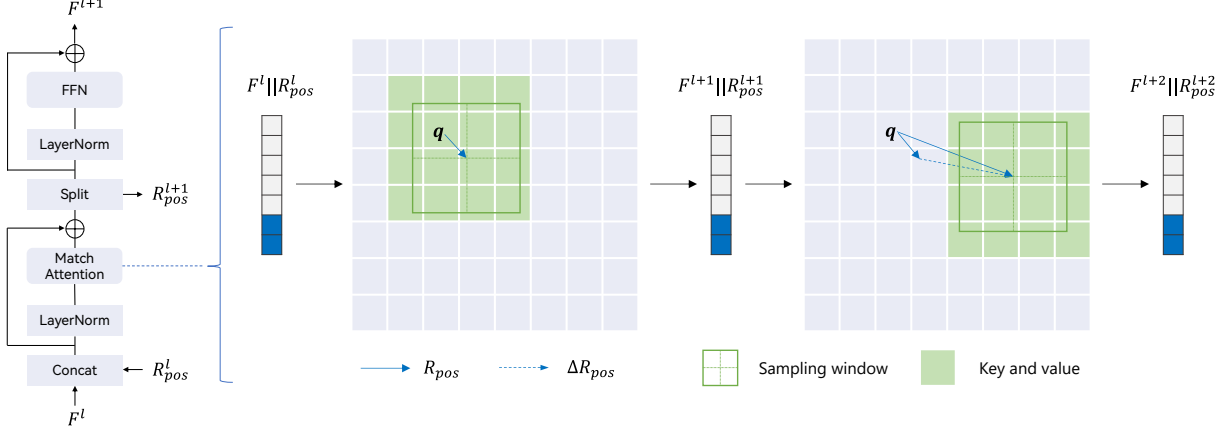


Fig. 1. MatchAttention block. *Left*: At the l -th layer of the transformer, the input feature tokens F^l and the relative position R_{pos}^l are concatenated in channel dimension and fed as input of MatchAttention after a LayerNorm. F^l and R_{pos}^l are updated by the residual connection which outputs F^{l+1} and R_{pos}^{l+1} , where the token features are further processed by a feed-forward network. *Center and right*: Between layers l and $l+1$, the relative position is updated dynamically. Here we illustrate with an effective 3×3 contiguous sampling window computed with its nearest 4×4 token window at discrete positions.

marks. MatchFlow-B also achieved state-of-the-art zero-shot performance on the high-resolution Spring [19] benchmark.

2 RELATED WORK

2.1 Attention Mechanism

The attention mechanism was first proposed for neural machine translation (NMT) [20]. The global attention is computed through all-pair correlations followed by softmax activation. Given a query token \mathbf{q}_i and key tokens $\{\mathbf{k}_j \mid j = 1, \dots, L\}$, the attention value is computed as

$$\alpha_{ij} = \frac{\exp(e_{ij})}{\sum_{k=1}^L \exp(e_{ik})}, \quad (1)$$

where $e_{ij} = \langle \mathbf{q}_i, \mathbf{k}_j \rangle$ denotes the similarity between \mathbf{q}_i and \mathbf{k}_j . For numerical stability, practical implementations subtract the maximum value $\hat{e}_i = \max_k e_{ik}$ from all e_{ik} ($k = 1, \dots, L$):

$$\alpha_{ij} = \frac{\exp(e_{ij} - \hat{e}_i)}{\sum_{k=1}^L \exp(e_{ik} - \hat{e}_i)}. \quad (2)$$

The exponential function significantly decreases the attention weights of tokens with non-maximum similarity. Consequently, global attention focuses on a sub-region centered around the maximum similarity token, resembling the core concept of ‘attention’. Although linear attention (without softmax activation) achieves a global receptive field with linear complexity, its inability to concentrate on specific sub-regions explains its inferior performance compared to global attention. This phenomenon can be verified through attention visualizations in [21].

We review three lines of work addressing the quadratic complexity of global attention while retaining softmax activation: (1) Sparse attention by exploring the sparsity of the attention matrix. Longformer [22] combines dilated sliding-window attention with global attention by introducing extra global tokens to form a mixed attention pattern with linear complexity, while Big Bird [23] enhances this pattern

by incorporating random attention. SparseK attention [24] further optimizes this paradigm by attending to the top- k key-value pairs for each query through input feature scoring and differentiable relaxation of the top- k operator; (2) Sliding-window attention that attends to a fixed-size sub-window for each query, commonly applied in vision domains. Neighborhood Attention (NAT) [25] attends to each query’s nearest neighbor tokens, thereby forming a local window. Its advantage over conventional local window attention lies in the handling of border tokens, as the latter relies on padding operations. When the window size aligns with the full token sequence length, NAT equates to global attention, whereas padded local window attention inevitably incurs information loss. CLEAR attention [26] adopts a circular sliding-window design, demonstrating improved performance in diffusion transformers. Swin Transformer’s shifted window attention [27] partitions tokens into non-overlapping sub-windows for parallel intra-window global attention. The shifted window paradigm enables cross-window connections, thereby expanding the effective receptive field. However, query-key connections within a single-layer remain confined to sub-window scales, rendering this approach unsuitable for cross-view matching tasks requiring long-range connections (e.g., large disparity or optical flow); (3) Deformable attention attends to a small subset of tokens by predicting offsets and pre-softmax attention weights for sampled tokens via the query feature. Tokens are sampled from contiguous locations through differentiable bilinear interpolation. This mechanism has been widely adopted in object detection [11] and BEV feature aggregation for autonomous driving [28].

In summary, sparse attention does not consider contiguous positions; sliding-window attention has fixed and non-dynamic sampling windows (center-aligned with the query or shifted); deformable attention lacks query-key similarity and predicts offsets from single-view features. All these properties are essential for cross-view matching, which can be addressed by the proposed MatchAttention.

2.2 Positional Embedding

The self-attention mechanism [29] is permutation invariant. To capture the order of token sequences, positional embeddings map discrete absolute positions i or relative positions $i - j$ into a contiguous vector space aligned with token embeddings, where i, j denote token indices. This mapping can employ fixed patterns or learnable parameters. Sinusoidal embeddings represent a fixed absolute encoding scheme capable of extrapolation to sequences longer than training data. Learnable positional embeddings [27], [30], [31] assign each absolute or relative position a parameterized vector representation, which can be efficiently looked up during inference. Rotary positional embedding (RoPE) [32] transforms input vectors through complex-space rotations, inherently encoding relative positions while maintaining rotation invariance. RoPE has been widely adopted in large language models [33] and 3D vision foundation models [1], [34]. Projective positional encoding (PRoPE) [35] captures camera intrinsics and extrinsics as a relative positional encoding, which shows improved performance in feed-forward novel view synthesis, stereo depth estimation and discriminative spatial cognition. STTR [36] demonstrates that relative positional embeddings in cross-attention layers enhance feature richness in texture-less regions for stereo matching.

In contrast with embedding position into a hidden vector space, the relative position in MatchAttention is contiguous and is used as is. For instance, the relative positions in self-MatchAttention can be inspected to verify occlusion handling. MatchAttention naturally embeds the relative position into the attention mechanism, where the relative positions are transformed and updated in the same way as the token features through concatenation.

2.3 High-Resolution Stereo Matching

High-resolution stereo matching can not only increase resolution and details but also reduce depth error, which is inversely proportional to focal length. However, the increased resolution also introduces several challenges, including expanded searching space, higher memory requirements, and larger computational costs. GC-Net [37] is the first end-to-end architecture employing 3D convolutions for cost volume filtering. PSMNet [38] subsequently advances this paradigm by introducing spatial pyramid pooling for multi-level feature extraction and stacked hourglass networks for advanced 3D CNN architectures. CoEx [39] leverages Guided Cost Volume Excitation (GCE), which utilizes image features to guide channel excitation of the cost volume, to improve 3D CNN efficiency while significantly reducing computational costs. Despite these advancements, 3D CNN methods often struggle to generalize beyond their training domains and remain computationally expensive at high resolutions due to the inherent complexity of 3D convolutions.

In contrast, groundbreaking approaches like RAFT [40] and RAFT-Stereo [15] employ cost volume lookup mechanisms, encoding sampled costs into features for iterative refinement of optical flow and disparity respectively. These methods compute the 4D/3D cost volume only once through matrix multiplication and exclusively use 2D convolutions, achieving remarkable memory and computational efficiency while maintaining applicability to high-

resolution imagery. RAFT-Stereo notably became the first deep learning method to surpass traditional stereo methods [41], [42] on the high-resolution Middlebury benchmark, demonstrating superior generalization through its iterative explicit matching strategy. IGEV-Stereo [43] enhances RAFT-Stereo’s framework by replacing the all-pair correlation volume with a geometry encoding volume (GEV) that employs a lightweight 3D UNet for cost volume filtering and regularization guided by image features. Furthermore, it initializes disparities from the combined GEV rather than zero, accelerating convergence and reducing refinement iterations. While effective, iterative updating mechanisms tend to aggregate global low-frequency information at the expense of high-frequency details. Selective-Stereo [44] addresses this limitation through a selective recurrent unit (SRU) that fuses high- and low-frequency GRU branches using spatial attention maps derived from contextual information. AIO-Stereo [45] extends this approach by integrating a dual-level knowledge utilization module that transfers knowledge from multiple vision foundation models (VFM) [46], [47], [48] into its context network. FoundationStereo [16] introduces a side-tuning adapter which integrates features from the monocular depth foundation model [48] to mitigate the sim-to-real gap. An attentive hybrid cost filtering (AHCF) module is also proposed for long-range cost aggregation. FoundationStereo can achieve strong zero-shot generalization through the proposed modules and the FoundationStereo (FSD) dataset.

The transformer architecture STTR [36] reformulates stereo matching as a sequence-to-sequence correspondence task using attention mechanisms with positional encoding, estimating disparities through optimal transport that enforces soft uniqueness constraints. UniMatch [5] employs a transformer with self- and cross-attention for cross-view feature aggregation, directly regressing disparities through simple feature correlations. Significantly, UniMatch’s architecture enables seamless application to stereo, optical flow, and depth estimation tasks with minimal parameter-free adaptations. Croco-Stereo [34] eliminates the requirement of cost volume by directly regressing disparities using a DPT head [49] from features extracted by a ViT [50] encoder-decoder pre-trained for cross-view completion. However, the lack of cost volume and explicit matching compromises its generalizability. Due to the global self- and cross-attention operations, Croco-Stereo incurs significant computational and memory overhead, requiring a tiling-based inference strategy that limits correspondence range and its applicability to high-resolution images.

Current iterative refinement methods [15], [43], [44] rely on static correlation volumes computed from initial features, which restricts their adaptability during refinement. Although updating these volumes could accelerate convergence, the prohibitive memory and computational costs of all-pair correlations present significant challenges. Our work bridges the gap between iterative refinement and transformer approaches by integrating explicit matching into attention mechanisms, enabling simultaneous iterative matching and feature aggregation.

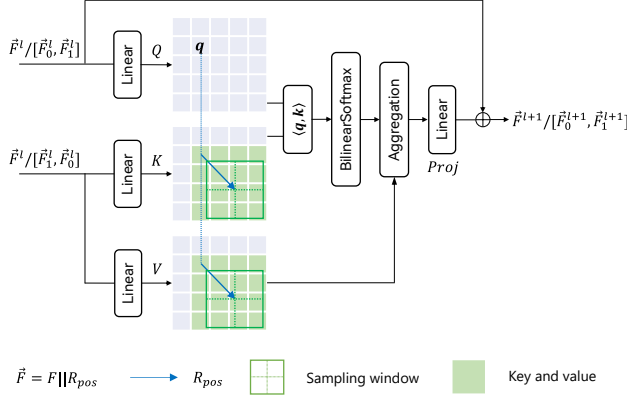


Fig. 2. MatchAttention mechanism. The input is defined as $\hat{F}^l = F^l || R_{pos}^l$ for self-MatchAttention or \hat{F}_0^l and \hat{F}_1^l concatenated along the batch dimension for cross-MatchAttention. For each query $q_i = Q[i, :]$, the sampling window is determined by $r_i = R_{pos}[i, :]$. Subsequently, three main operations are performed within the sampling window: (1) query-key similarity computation, (2) BilinearSoftmax, and (3) value aggregation. Finally, the relative position is updated in tandem with token features via the residual connection.

3 MATCHATTENTION: MATCHING THE RELATIVE POSITION

An illustration of MatchAttention is shown in Figure 2. For self-MatchAttention, the input consists of concatenated token features and relative positions $\hat{F} = F || R_{pos}$ from a single view, where $||$ denotes channel-wise concatenation. For cross-MatchAttention, inputs \hat{F}_0 and \hat{F}_1 from the reference and target views are transformed into query (Q), key (K), and value (V) representations as follows:

$$\begin{aligned} Q &= W_q \hat{F}_0, \\ K &= W_k \hat{F}_1, \\ V &= W_v \hat{F}_1, \end{aligned} \quad (3)$$

where W_q , W_k , and W_v are weight matrices of the linear layers. When reversing the input order to \hat{F}_1 and \hat{F}_0 , cross-MatchAttention from the reference to target view can also be computed. The positive and reverse order inputs are concatenated in the batch dimension ($[\hat{F}_0, \hat{F}_1]$ and $[\hat{F}_1, \hat{F}_0]$) to compute the results of both views in parallel.

Given a query $q_i = Q[i, :]$, the corresponding sampling window center for keys and values is computed as $p_i^k = p_i^q = p_i^v + r_i$, where $r_i = R_{pos}[i, :]$. For an effective sampling window \mathcal{W}_i of size w^2 , there exists an expanded sampling window $\bar{\mathcal{W}}_i$ of size $(w+1)^2$ at the discrete location $\lfloor p_i^k \rfloor$. The similarity between q_i and keys k_j within $\bar{\mathcal{W}}_i$ is computed. With the query-key similarities $\langle q_i, k_j \rangle$ for $j \in \bar{\mathcal{W}}_i$ and the relative position r_i , BilinearSoftmax outputs attention weights $\bar{\alpha}_{ij}$ corresponding to tokens within $\bar{\mathcal{W}}_i$, which will be described in detail in Section 3.1. Finally, the value tokens $\{v_j | j \in \bar{\mathcal{W}}_i\}$ are aggregated using the attention weights $\bar{\alpha}_{ij}$ and projected to the output space via a linear projection layer with weight matrix W_p . The mathematical formulation of MatchAttention will be provided in Section 3.2. In Section 3.3, the computational complexity of MatchAttention is analyzed.

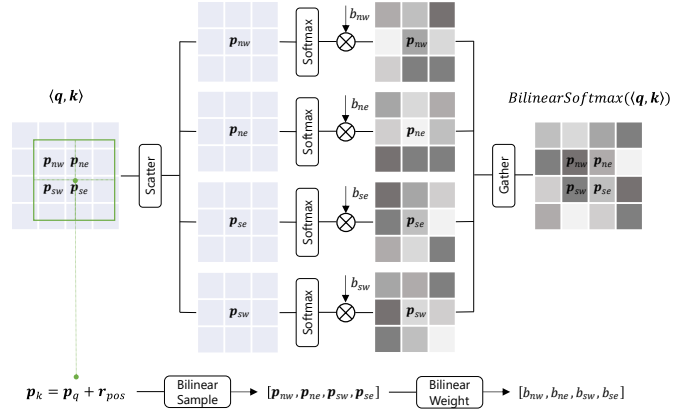


Fig. 3. BilinearSoftmax consists of bilinear sampling of p_k , scattering the sampled points from the expansion window $\bar{\mathcal{W}}$ into four sub-windows (\mathcal{W}_{nw} , \mathcal{W}_{ne} , \mathcal{W}_{sw} , \mathcal{W}_{se}), computing softmax within sub-windows, multiplying bilinear weights, and then gathering to obtain the final attention weights. The subscript i is omitted for simplicity.

3.1 BilinearSoftmax

BilinearSoftmax enables contiguous and differentiable attention sampling. As shown in Figure 3, the center of the sampling window \mathcal{W}_i is determined by:

$$p_i^k = p_i^q + r_i, \quad (4)$$

where p_i^q represents the position of q_i , and $r_i = R_{pos}[i, :]$. The resulting position p_i^k is contiguous and can be rounded into $\lfloor p_i^k \rfloor$; its nearest integer positions are obtained by bilinear sampling, where $p_i^{nw} = \lfloor p_i^k \rfloor$. Using the integer positions p_i^{nw} , p_i^{ne} , p_i^{sw} , p_i^{se} as centers, four sub-windows \mathcal{W}_i^{nw} , \mathcal{W}_i^{ne} , \mathcal{W}_i^{sw} , \mathcal{W}_i^{se} of the same size w can be scattered from the expanded window $\bar{\mathcal{W}}_i$ of size $(w+1)^2$. Softmax operations are then performed within each sub-window, and the resulting attention weights are multiplied by corresponding bilinear weights b_i^{nw} , b_i^{ne} , b_i^{sw} , b_i^{se} before being gathered back into $\bar{\mathcal{W}}_i$. The final output of BilinearSoftmax consists of attention weights $\{\bar{\alpha}_{ij} | j \in \bar{\mathcal{W}}_i\}$ at discrete locations.

BilinearSoftmax effectively reassembles the attention of q_i to keys at contiguous locations within \mathcal{W}_i , while computing at discrete positions. BilinearSoftmax is differentiable because all operations shown in Figure 3, including bilinear sampling, scattering, softmax, multiplication, and gathering, are differentiable. To optimize memory usage, we fuse these operations into a single CUDA kernel by taking the advantage of window overlapping, which avoids storing the attention weights of sub-windows and addresses potential memory bottlenecks at high resolution.

An alternative method is directly sampling keys and values within \mathcal{W}_i by bilinear interpolation and computing attention weights by softmax. However, this approach introduces a $4\times$ increase in computational cost for both query-key similarity calculations and value aggregation operations. In contrast, our optimized method leverages window overlapping to ensure each query-key/value pair is computed only once. The computational cost associated with bilinear sampling applies specifically to BilinearSoftmax. Specifically, bilinear sampling of attention weights is more efficient than that of key/value features because weights are

scalar values, whereas features are vectors. This inherent efficiency further underscores the benefits of our proposed method.

3.2 Formulation

MatchAttention is a variant of sliding-window attention which attends to a dynamic and contiguous sampling window for each query. In contrast to the simple yet elegant matrix multiplication operation in global attention [29], we employ a per-query formulation. Given Q, K, V in (3) and R_{pos} , the attention for the i -th query is computed as

$$\begin{aligned} MatchAttention_w(Q, K, V, R_{pos})[i] &= W_p \mathbf{m}_i \\ &= W_p \sum_{j \in \bar{\mathcal{W}}_i} BilinearSoftmax(\langle \mathbf{q}_i, \mathbf{k}_j \rangle) \mathbf{v}_j, \end{aligned} \quad (5)$$

where $\bar{\mathcal{W}}_i = \{\lfloor \mathbf{p}_i^k \rfloor + (u, v) \mid u, v = -w/2, \dots, w/2 + 1\}$, \mathbf{m}_i is obtained by aggregating values $\{\mathbf{v}_j \mid j \in \bar{\mathcal{W}}_i\}$ using attention weights $\{\alpha_{ij} = BilinearSoftmax(\langle \mathbf{q}_i, \mathbf{k}_j \rangle)\}$, and

$$\begin{aligned} BilinearSoftmax(\langle \mathbf{q}_i, \mathbf{k}_j \rangle) &= \sum_{t \in \mathcal{T}} b_i^t \times Softmax(\langle \mathbf{q}_i, \mathbf{k}_{j^t} \rangle), \\ &= \sum_{t \in \mathcal{T}} b_i^t \times \alpha_{ij^t}^t, \\ &= \sum_{t \in \mathcal{T}} b_i^t \times \frac{\exp(\langle \mathbf{q}_i, \mathbf{k}_{j^t} \rangle)}{\sum_{j' \in \mathcal{W}_i^t} \exp(\langle \mathbf{q}_i, \mathbf{k}_{j'} \rangle)}, \\ &= \sum_{t \in \mathcal{T}} \frac{b_i^t}{Z_i^t} \exp(\langle \mathbf{q}_i, \mathbf{k}_{j^t} \rangle), \end{aligned} \quad (6)$$

where $\mathcal{T} = \{nw, ne, sw, se\}$, $j^t \in \mathcal{W}_i^t \subset \bar{\mathcal{W}}_i$, and $\mathcal{W}_i^t = \{\mathbf{p}_i^t + (u, v) \mid u, v = -w/2, \dots, w/2\}$. j^t may be empty if j is on the border of $\bar{\mathcal{W}}_i$.

The query-key similarity $\langle \mathbf{q}_i, \mathbf{k}_j \rangle$ can be arbitrarily defined. For cross-view matching, a point in the reference view has only one ground-truth correspondence in the target view, implying the sparse nature of matching. Therefore, we propose using the *negative L1-norm* as the similarity measure to enforce sparseness, which can be combined with softmax as

$$Softmax(\langle \mathbf{q}_i, \mathbf{k}_j \rangle) = \frac{1}{Z_i} \exp(-\gamma \|\mathbf{q}_i - \mathbf{k}_j\|_1), \quad (7)$$

where $\gamma = 1/\sqrt{c_k}$, c_k is the channel dimension of queries and keys. The combined softmax and negative L1-norm forms a normalized Laplace kernel, which can aid extracting edges and details. There is theoretical analysis [51] showing that transformers are equivalent to support vector machines (SVMs) under dot-product similarity. We believe that the normalized Laplace kernel formulation can further bridge the relationship between transformers and SVMs.

The relative positions are updated by the residual connections in the forward pass and its learnable parameters are encoded in the two additional channels of $W_q \in \mathbb{R}^{(c_{in}+2) \times c_k}$, $W_k \in \mathbb{R}^{(c_{in}+2) \times c_k}$, $W_v \in \mathbb{R}^{(c_{in}+2) \times c_v}$, and $W_p \in \mathbb{R}^{c_v \times (c_{out}+2)}$, where c_{in} and c_{out} represent the input and output feature channels. The backward gradient of the relative position is not only propagated by the residual connection but also by the bilinear weights $\{b_i^t\}$ of the

bilinear sample operator of BilinearSoftmax. The gradient of b_i^t is

$$\begin{aligned} \frac{\partial \mathcal{L}}{\partial b_i^t} &= \sum_{j^t \in \mathcal{W}_i^t} \frac{\partial \mathcal{L}}{\partial \bar{\alpha}_{ij^t}} \times \alpha_{ij^t}^t, \\ &= \sum_{j^t \in \mathcal{W}_i^t} \frac{\partial \mathcal{L}}{\partial \bar{\alpha}_{ij^t}} \times \frac{1}{Z_i^t} \exp(-\gamma \|\mathbf{q}_i - \mathbf{k}_{j^t}\|_1), \end{aligned} \quad (8)$$

which is propagated by the matching relations within \mathcal{W}_i^t .

Multi-head MatchAttention is implemented by splitting the feature channels into the number of heads h , which can be processed in parallel following [29]. For self-MatchAttention, each head is assigned different relative positions such that the model can attend to different positions jointly. For cross-MatchAttention, all heads share the same relative positions because the matching relation is one-to-one and determined for cross-view matching.

Note that w in (5) does not introduce learnable parameters. Therefore, one can train with large w and use small w for inference with the same model weights.

3.3 Complexity Analysis

As shown in Figure 2, the MatchAttention mechanism comprises parameter and non-parameter modules. The parameter modules are linear layers with linear complexity, which attribute to Tensor FLOPs. We analyze the complexity of the non-parameter modules: query-key similarity, BilinearSoftmax, and value aggregation. Since the relative position is dynamic and not center-aligned with the query, the non-parameter modules are attributed to the general purpose CUDA FLOPs. Assume the query, key, and value tokens have the same size $H \times W$, the FLOPs of the query-key similarity module is $H \times W \times h \times c_k \times (w+1)^2 \times 2$; the FLOPs of the BilinearSoftmax module is $H \times W \times h \times (20 + (w+1)^2 \times 2 + w^2 \times 4 \times 3)$; the FLOPs of the attention aggregation module is $H \times W \times h \times c_v \times (w+1)^2 \times 2$. Therefore, the overall computational complexity is $O(HWh \max(c_k, c_v)w^2)$. Given that w is a small constant (e.g., 3 or 5 in MatchDecoder), the complexity of MatchAttention scales linearly with the number of tokens $H \times W$.

The memory required to store attention values is $H \times W \times h \times (w+1)^2$, which scales linearly with token size and is smaller than the memory required to store token features if $(w+1)^2 < \max(c_k, c_v)$.

4 MATCHATTENTION FOR CROSS-VIEW MATCHING

The relative position $\mathbf{r}_i = \mathbf{p}_i^k - \mathbf{p}_i^q = R_{pos}[i, :]$ is exactly the learning target for cross-view matching, which represents flow for optical flow, and its x -component can serve as disparity for stereo matching.

R_{pos} can be effectively estimated by MatchAttention. As illustrated in Figure 4, given token features F_0^l, F_1^l , and relative positions $R_{pos,0}^l, R_{pos,1}^l$ from the reference and target views, the query tokens are matched with key tokens within a sampling window centered at \mathbf{p}_i^k . Value features are then aggregated from the target view to the reference view and added with the input feature of the reference view to produce updated features F_0^{l+1} and relative positions

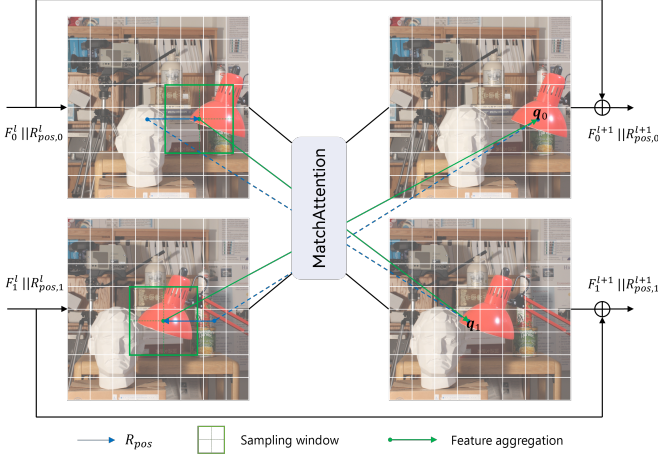


Fig. 4. Cross-view matching and feature aggregation. For a given query in the reference view, its matching window in the target view is computed by the relative position. Features within the matching window are aggregated from the target view to the reference view via MatchAttention and added to the input features of the reference view through the residual connection.

$F_{pos,0}^{l+1}$. This process operates in both directions, and through residual connections, features and relative positions of both views are iteratively updated.

We design a hierarchical cross-view decoder termed as MatchDecoder in Section 4.1 using self- and cross-MatchAttention as building blocks. To address the fundamental challenge of occlusion in cross-view matching, in the forward pass we propose explainable occlusion handling by improving self- and cross-MatchAttention respectively in Section 4.2. In the backward pass, we propose consistency-constrained loss in Section 4.3 to avoid the negative impact of occlusion on training. The final improved model is termed as MatchStereo for stereo matching and MatchFlow for optical flow.

4.1 Hierarchical Cross-View Decoder

We adopt a hierarchical coarse-to-fine design for efficiency, as shown in Figure 5. The details of MatchDecoder are as follows.

Encoder. Given input images I_0 and I_1 of the reference and the target views, the encoder extracts features at multiple scales $\{s \mid s = 1/4, 1/8, 1/16, 1/32\}$. Its basic blocks consist of separable convolutions [52] and MLP with GELU [53] activation.

UpConv and Convex Upsample. The features are upsampled by the UpConv module of U-Net [54] from $1/32$ to $1/4$ scales iteratively. Relative position R_{pos} is upsampled by the convex upsample module, which is introduced in RAFT [40] for optical flow upsampling.

Initial Correlation. The initial R_{pos} is computed by correlating features F_0 and F_1 at $1/32$ scale. To stabilize the training F_0 and F_1 are normalized by layer normalization and transformed by two different linear layers before the correlation.

For optical flow, the correlation matrix is computed as $C_{flow} = \text{Softmax}(F_0 F_1^T / \sqrt{c}) \in \mathbb{R}^{H \times W \times H \times W}$, where c is the feature channels and softmax is taken over the last two dimensions. For stereo matching, the correlation is along the

epipolar line (x -axis) for rectified stereo pairs. The correlation matrix $C_{disp} \in \mathbb{R}^{H \times W \times W}$ is converted to a cost volume $V_{disp} \in \mathbb{R}^{H \times W \times D}$ by shifting, where $D = W$. Instead of regressing flow or disparity using the full coordinate grid or disparity range [5], the initial flow/disparity is regressed within a local window with size $k = 5$, where the window center corresponds to the maximum probability of averaged $\tilde{C}_{flow} / \tilde{V}_{disp}$ with the same window size. The initial flow is exactly the initial relative position for optical flow. The initial relative position for stereo matching is defined as

$$R_{pos,0} = -\mathbf{d}_0 || \mathbf{0}, R_{pos,1} = \mathbf{d}_1 || \mathbf{0}, \quad (9)$$

where \mathbf{d}_0 and \mathbf{d}_1 are positive and a negative sign is assigned to the reference view \mathbf{d}_0 for correct matching relations.

MatchAttention Block. MatchAttention block consists of interleaved self-MatchAttention, cross-MatchAttention, and convolutional gated linear units (ConvGLU) [31].

For self-MatchAttention, the self relative position sR_{pos} is initialized as zero and upsampled by the same convex upsample module as R_{pos} . We also feed the cross-view R_{pos} to the input of self-MatchAttention, $\hat{F} = F || R_{pos} || sR_{pos}$, enabling refinement of R_{pos} by monocular features. Here sR_{pos} is utilized for attention sampling within MatchAttention, while R_{pos} serves as two additional feature channels of F .

For cross-MatchAttention, the input is $\hat{F} = F || R_{pos}$. By the concatenation operation, both token features and relative positions can be explicitly matched. We further add the flattened attention weights $\bar{\alpha}_i = \{\bar{\alpha}_{ij} \mid j \in \bar{W}_i\}$ to the input of the linear projection layer and Equation 5 becomes

$$W'_p(\mathbf{m}_i || \bar{\alpha}_i), \quad (10)$$

where $W'_p \in \mathbb{R}^{(c_v + (w+1)^2) \times (c_{out} + 2)}$. The attention weights $\bar{\alpha}_i \in \mathbb{R}^{(w+1)^2}$ can be interpreted as local matching costs and improve matching performance, though this breaks the property that the size of learnable parameters is independent of w . Adding $\bar{\alpha}_i$ to the projection layer is optional and not used for self-MatchAttention.

There may be unreliable matchings in textureless regions and there is no ground-truth matchings in occluded regions. In such cases, the features aggregated from the sampling window should be filtered out. The gated mechanism of ConvGLU [31] can filter out the unreliable features and therefore it is adopted as the feed-forward network to improve feature representation. Moreover, the depth-wise convolution of ConvGLU can serve as a conditional position embedding [55], which accommodates the local position information within the sampling window.

4.2 Explainable Occlusion Handling

Given a query token \mathbf{q}_i from occluded regions of the reference view, there is no correspondence in the target view. If using ground-truth $\mathbf{r}'_i = R_{pos,0}^{gt}[i, :]$ for feature aggregation, the foreground features of the target view will be mistakenly aggregated into the occluded \mathbf{q}_i , which will cause feature ambiguity and affect subsequent matching. To address this, we introduce gated cross-MatchAttention and Equation 10 further becomes

$$W'_p((\mathbf{g}_i \odot \mathbf{m}_i) || \bar{\alpha}_i), \quad (11)$$

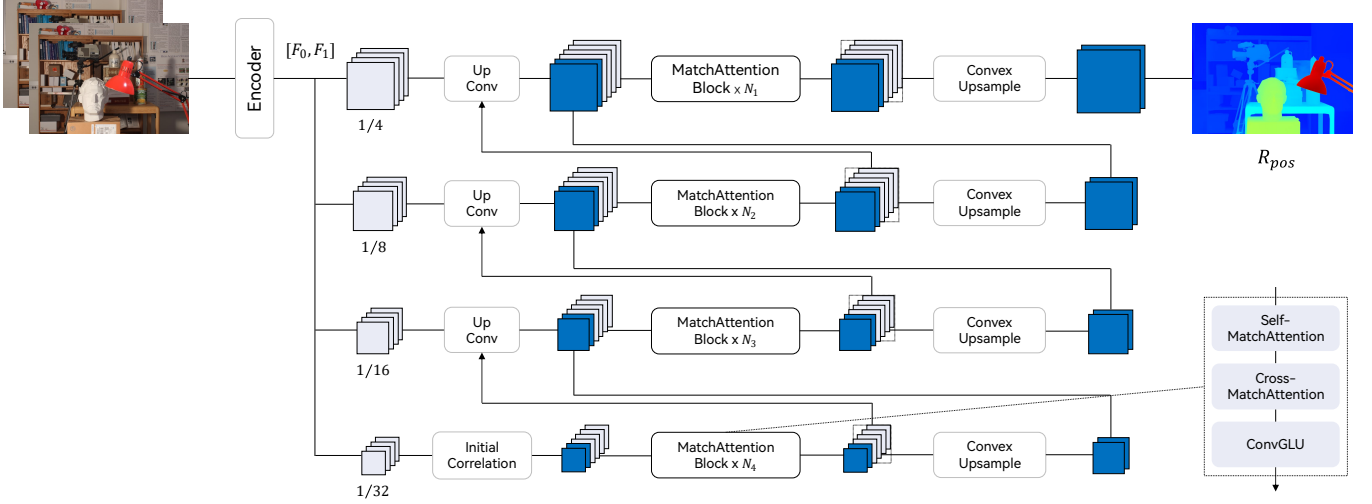


Fig. 5. MatchDecoder architecture. Given cross-view inputs I_0 and I_1 , the encoder extracts features at scales $s = 1/4, 1/8, 1/16, 1/32$. Initial correlation estimates the initial R_{pos} at $1/32$ scale. R_{pos} is iteratively refined by the MatchAttention block that consists of self-MatchAttention, cross-MatchAttention, and ConvGLU [31]. The final output R_{pos} is upsampled from $1/4$ scale to full resolution using convex upsample [40].

where $\mathbf{g}_i = G[i, :]$, $G = \text{SiLU}(W_g \hat{F}_0)$ is learned from the reference view features \hat{F}_0 with SiLU [56] activation, $W_g \in \mathbb{R}^{(c_{in}+2) \times c_k}$. The gated mechanism can filter out unreliable aggregated feature \mathbf{m}_i by \mathbf{g}_i , especially for \mathbf{q}_i in occluded regions.

To refine $\mathbf{r}_i = R_{pos}[i, :]$ in occluded regions, as mentioned above, R_{pos} is concatenated as two additional feature channels to the input of self-MatchAttention to leverage monocular cues. Furthermore, since $R_{pos,0}$ and $R_{pos,1}$ of the reference and target views can be estimated simultaneously ($R_{pos} = [R_{pos,0}, R_{pos,1}]$), the non-occlusion mask of the current layer can be calculated by consistency check

$$\begin{aligned} R_{pos,0}^{1 \rightarrow 0} &= \mathcal{B}(R_{pos,1}, R_{pos,0} + G_{2D}), \\ M_{noc,0} &= \|R_{pos,0} + R_{pos,0}^{1 \rightarrow 0}\|_1 \leq A, \end{aligned} \quad (12)$$

where $R_{pos,0}^{1 \rightarrow 0}$ is sampled from $R_{pos,1}$ using coordinate grid $R_{pos,0} + G_{2D}$ by the bilinear sample operator \mathcal{B} and A is a threshold. This formulation exploits the geometric property that corresponding points exhibit inverse relative positions ($R_{pos,0} = -R_{pos,0}^{1 \rightarrow 0}$) in non-occluded regions. $M_{noc,1}$ can be calculated similarly and $M_{noc} = [M_{noc,0}, M_{noc,1}]$.

We embed the non-occlusion mask M_{noc} as an additional feature channel of the self-MatchAttention input $\hat{F}' = F \parallel R_{pos} \parallel sR_{pos} \parallel M_{noc}$ to achieve the perception of occluded regions during refinement. Note M_{noc} is not involved in residual connection and backward gradient propagation.

By inspecting the self relative position sR_{pos} in self-MatchAttention, we can visualize the sampling window locations of the occluded regions. As shown in Figure 6 which shows the x -component of sR_{pos} for stereo matching, the sR_{pos-x} of background occluded regions is negative, meaning the sampling window is at left-side non-occluded neighboring regions. For border occluded regions on the left of the reference image, sR_{pos-x} is positive, indicating that the sampling window is at right-side non-occluded neighboring regions.

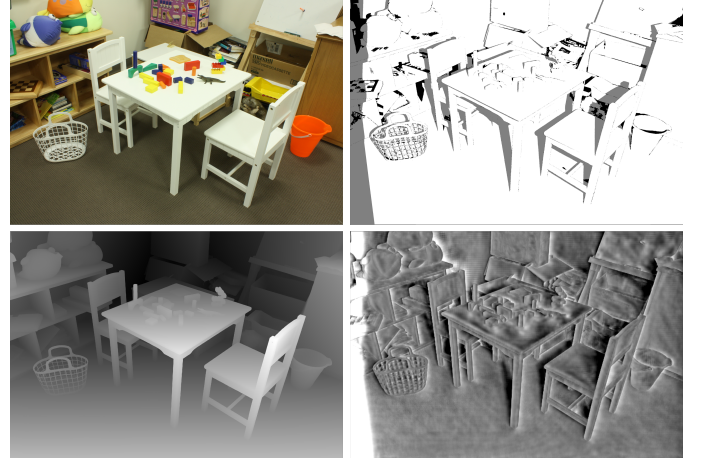


Fig. 6. Visualization of self relative positions. Top: Color reference image (from Middlebury [12] full resolution dataset) and ground-truth non-occlusion mask (grey color means occluded). Bottom: Zero-shot disparity map and sR_{pos-x} (range from -35.8 to 145.9) predicted by MatchStereo-B trained on FSD Mix dataset.

Therefore, the network can learn to interpolate occluded regions using neighboring non-occluded regions. As shown in the next section, the explainable occlusion handling is learned without explicit supervision of occlusion.

4.3 Consistency-Constrained Loss

In cross-view matching the supervision on occluded regions using ground-truth will force the occluded regions in the reference view to be matched with the foreground regions in the target view, which affects the network’s learning of normal matching relationships. To address this problem, we propose a consistency-constrained supervision strategy such that the network can learn matching relations on non-occluded regions only.

The loss function is supervised over all intermediate relative positions of the reference view

$$\mathcal{L} = \mathcal{L}_{init} + \mathcal{L}_{self} + \mathcal{L}_{cross}[\mathcal{M}_{noc,0}], \quad (13)$$

where \mathcal{L}_{init} is the loss for the initial R_{pos} , \mathcal{L}_{self} is the loss for the R_{pos} of self-MatchAttention and convex upsample, \mathcal{L}_{cross} is the loss for the R_{pos} of cross-MatchAttention. $\mathcal{M}_{noc,0}$ represents the set of non-occlusion masks $\{M_{noc,0}^l \mid l = 1, \dots, N\}$, where $N = N_1 + N_2 + N_3 + N_4$.

\mathcal{L}_{init} is defined as $\|R_{pos,0}^{gt} - R_{pos,0}^{init}\|_1$ for optical flow and the multi-modal cross-entropy loss [57] supervised on the initial cost volume $V_{disp,0}$ for stereo matching.

\mathcal{L}_{self} and \mathcal{L}_{cross} are defined as the sum of sub-layer losses with exponential increasing weights

$$\mathcal{L}_{self} = \sum_{l=1}^{N_s} \gamma^{N_s-l} L_{self}^l, \mathcal{L}_{cross} = \sum_{l=1}^N \gamma^{N-l} L_{cross}^l, \quad (14)$$

where γ is a discount factor, $N_s = N + 4$ accounts for four additional convex upsampling layers. L_{self}^l is defined as L1 loss

$$L_{self}^l = \|R_{pos,0}^{gt} - R_{pos,0}^{l,self}\|_1, \quad (15)$$

and L_{cross}^l is defined as

$$L_{cross}^l = \| (R_{pos,0}^{gt} - R_{pos,0}^{l,cross}) \cdot M_{noc,0}^l \|_1 + \epsilon \| (R_{pos,0} + R_{pos,0}^{1 \rightarrow 0}) \cdot M_{noc,0}^l \|_1, \quad (16)$$

where the first term is L1 loss on the non-occlusion mask, and the second term is the consistency loss multiply with a small constant ϵ .

By incorporating the non-occlusion masks $\mathcal{M}_{noc,0}$ for cross-MatchAttention, inconsistent and unreliable matches can be filtered out from the supervision. The loss \mathcal{L} exclusively utilizes left-view ground-truth disparity/flow, which eliminates the need for ground-truth non-occlusion masks or those derived from cross-view consistency checks between ground-truth of both views.

5 EXPERIMENT

5.1 Experiment Setting

5.1.1 Implementation Details

The proposed MatchDecoder is implemented in Pytorch with custom CUDA kernels for MatchAttention, and a pure PyTorch version is also available. R_{pos} for cross-MatchAttention is multiplied with a learnable parameter $\beta \in \mathbb{R}^2$ before concatenated with token features to balance their scales and stabilize the gradients during training, β is initialized as (0.1, 0.1). A in Equation 12 is set as 1 and ϵ in Equation 16 is set as 0.01.

For all the experiments, we train MatchStereo / MatchFlow (MatchDecoder applied to specific tasks) using AdamW optimizer [58] with weight-decay 0.05, learning rate $5e-4$, and one-cycle learning rate schedule. The crop-size is 416×832 and the data augmentation of RAFT-Stereo [15] and RAFT [40] are adopted for stereo and flow, respectively. All the models are trained from scratch without weight initialization from pre-trained models.

Stereo Matching. For the zero-shot evaluation, MatchStereo is trained on Scene Flow [14] for 200k steps with batch

size 32. MatchStereo is also trained on the FSD Mix dataset (including FSD [16], Scene Flow [14], Sintel [59], CREStereo [60], FallingThings [61], InStereo2K [62], and HR-VS [63]) for 500k steps with batch size 32, denoted as MatchStereo-B (FSD Mix). For the ablation study, MatchStereo-B is trained on Scene Flow for 100k steps with batch size 16. For the benchmark evaluation on Middlebury [12] and ETH3D [13], MatchStereo-B (FSD Mix) is further finetuned on a mixed dataset of FSD Mix and the target datasets for 100k and 50k steps, respectively. For the benchmark evaluation on KITTI 2012 [17] and KITTI 2015 [18], MatchStereo-B (FSD Mix) is further finetuned on the mixed datasets of KITTI 2012, KITTI 2015, and Virtual KITTI 2 [64] for 100k steps.

Optical Flow. Similarly, for the zero-shot evaluation on Sintel [59] and KITTI 2015 [18], MatchFlow-B is trained on Scene Flow [14] for 100k steps with batch size 32. We do not follow the C + T protocol (FlyingChairs [65] + FlyThings3D [14]) since the resolution of FlyingChairs (384×512) is much lower than the training crop size (416×832). For the zero-shot evaluation on Spring [19], MatchFlow-B is further finetuned on a mixed dataset of Scene Flow [14], Sintel [59], KITTI 2015 [18], and HD1K [66] for 100k steps.

5.1.2 Benchmark Datasets and Evaluation Metrics

Benchmark Datasets. Four real-world benchmark datasets are utilized for stereo matching evaluation. The Middlebury V3 benchmark [12] provides online evaluation of stereo methods with high-resolution ground-truth captured by a structure light system. It consists of indoor scenes with challenges of low or repetitive textures, different lighting conditions, large occlusions, and imperfect rectification. KITTI 2012 [17] and KITTI 2015 [18] datasets consist of outdoor driving scenes with sparse ground-truth obtained from LIDAR sensors. ETH3D [13] dataset consists of low-resolution indoor and outdoor stereo image pairs.

Sintel [59], KITTI 2015 [18], and Spring [19] datasets are selected for benchmarking optical flow performance.

Evaluation Metrics. For stereo matching, '> Xpx' represents the percentage of pixels whose disparity error larger than X pixels. 'AvgErr' represents the average disparity error of all pixels. 'D1' represents the percentage of outlier whose disparity error larger than 3 pixels and 5% of the ground-truth. 'Noc' represents the non-occluded region mask and 'All' represents the all region mask. For optical flow, 'EPE' represents endpoint error under L2 distance. 'Fl-all' represents the percentage of outlier whose flow error larger than 3 pixels and 5% of the ground-truth.

5.2 Model Architectures and Inference Performance

5.2.1 Model Architectures

We propose three architecture variants for MatchStereo / MatchFlow, tiny (-T), small (-S), and base (-B). The detail configurations are listed in Table 1. The three variants -T, -S, and -B have the only difference of feature channels. At $1/4$ scale, only $N_1 = 2$ MatchAttention Blocks are enough to obtain satisfactory results. This is a huge computational saving in contrast with methods using RAFT-like [40] GRU disparity decoders (e.g., FoundationStereo [16], AIO-Stereo [45], DEFOM-Stereo [67], Selective-IGEV [44]) where 32 GRU iterations are required at inference. In addition, the

TABLE 1

Architecture details of MatchDecoder. The encoder scales are from 1/4 to 1/32 and the decoder scales are from 1/32 to 1/4.

Architecture details	MatchStereo / MatchFlow
Encoder depths	(2, 2, 6, 2) -T (32, 64, 128, 160)
Encoder channels	-S (64, 128, 160, 320) -B (128, 256, 320, 512)
MLP ratio	2
Decoder depths	(8, 8, 8, 2) -T (160, 128, 64, 32)
Decoder channels	-S (320, 160, 128, 64) -B (512, 320, 256, 128)
Window sizes	(5 × 5, 5 × 5, 3 × 3, 3 × 3)
Num heads	4
ConvGLU ratio	2

TABLE 2

Inference performance comparison of MatchAttention and the global attention [29] (linear layers are not included). Both tested with 256 feature channels and FP32 precision.

Methods	Token resolution	Memory (MB)	Latency (ms)
Global attention	196 × 196	17630	27.9
MatchAttention	196 × 196	870	1.4
	512 × 512	2448	4.2
	768 × 768	4652	7.7
	1024 × 1024	7804	12.5
	2048 × 2048	29464	43.1

small sampling window size 3×3 at 1/8 and 1/4 scales makes the attention sampling efficient.

5.2.2 Inference Performance

We first compare the inference performance of MatchAttention and the global attention [29] evaluated on a single RTX 5090 GPU. As listed in Table 2, MatchAttention has 20.3× memory reduction and 19.9× latency speed up compared with the global attention at token resolution 196×196 . GPU out-of-memory (OOM) is incurred at token resolution 256×256 for the global attention. In contrast, MatchAttention can support up to 2048×2048 token resolution. Moreover, the memory and latency of MatchAttention scales approximately linearly with respect to the token resolution.

The inference performance of MatchStereo is compared with RAFT-Stereo [15] and FoundationStereo [16] since RAFT-Stereo is the base architecture for RAFT-like iterative refinement methods and FoundationStereo has SOTA accuracy and zero-shot generalization ability. The inference profiling is shown in Table 3. MatchStereo-S has 4.5× memory reduction and 4.8× speed up compared to RAFT-Stereo and MatchStereo-B has 6.7× memory reduction and 10.3× speed up compared to FoundationStereo under the same resolution (1536×1536). For reference, MatchStereo-B is faster than the SOTA monocular depth estimation method DepthPro [68]. MatchFlow-B has similar computational cost with MatchStereo-B with the only difference at the 1/32 scale initial correlation. Note that the general purpose CUDA FLOPs contributed by the non-parameter modules of MatchAttention amount to only 4.6%, 2.8%, 1.4% of the total FLOPs for the -T, -S, and -B variants.

Furthermore, MatchStereo-T has 1/81 FLOPs, $5.1 \times$ memory reduction, and $6.8 \times$ speed up compared to RAFT-Stereo. With torch.compile enabled and inference at half precision, MatchStereo-T can achieve real-time latency for high-resolution images (38ms for 1536×1536 resolution) and can process 4K UHD (2176×3840) images in less than 0.1 seconds. The efficiency is achieved without sacrificing accuracy as shown in Section 5.4 and Section 5.5.

5.3 Ablation Study

The ablation study validates the effectiveness of four key components (L, A, G, N) build upon the baseline MatchDecoder architecture through comprehensive experiments on the real-world Middlebury dataset across three resolutions: F (full resolution), H (half resolution), and Q (quarter resolution). All model variants are trained on the synthetic Scene Flow [14] dataset. The results are listed in Table 4.

Baseline Architecture. The baseline architecture refers to the basic MatchDecoder illustrated in Figure 5, with the proposed MatchAttention Block as its core component. It represents the fundamental cross-view matching framework without the subsequent improvements (L, A, G, N). Importantly, even this baseline architecture achieves good performance across all resolutions, demonstrating the inherent effectiveness of the MatchAttention mechanism for cross-view matching.

Consistency-Constrained Loss (L): The additive experiment Baseline + L shows performance improvement at half and quarter resolution while degradation at full resolution, suggesting that the consistency constraint may interfere with fine-grained matching when abundant detail is available. However, the subtractive ablation Full - L validates its contribution to the final model at all resolutions. This contradiction can be explained through training dynamics: when L is trained jointly with other components (A, G, N) in the full model, the consistency constraint learns to complement other mechanisms and focuses on regulating correspondences in ambiguous regions.

Attention Weights as Additional Input (A): This component shows increasing effectiveness as resolution decreases with 25% improvement for ‘Q, All’. This validates that attention weights can serve as local matching costs and provide correspondence cues when pixel-level detail is limited, while being less critical when abundant detail is available.

Gated Cross-MatchAttention (G): This component also shows increasing effectiveness as resolution decreases, which demonstrates that filtering unreliable correspondences becomes increasingly important as resolution decreases and fine details are lost.

Non-Occlusion Mask Embedding (N): This component shows improved performance at full and quarter resolution and degraded performance at half resolution in both the additive and subtractive experiments. We analyze the reason is incorrect running non-occlusion mask may affect feature representation. This component is marked as *optional* since it is not necessary for occlusion filtering but serve as additional cues for the interpolation of occluded regions.

Low Resolution Initialization (LRI): The input images are first resized to 1/2 or 1/4 resolution and processed through MatchDecoder to obtain initial relative position

TABLE 3

Inference profiling including latency, memory, Tensor FLOPs (matrix matmul), and CUDA FLOPs (general purpose). By default, all methods are evaluated with native Pytorch and FP32 precision except FoundationStereo, which is evaluated with mixed precision (\dagger) due to memory limitation. The results within the parenthesis show the memory and latency with torch.compile enabled and inference at half precision.

Methods	Params	Resolution	CUDA FLOPs	Tensor FLOPs	Memory (MB)	Latency (ms)
DepthPro [68]	952M	1536 \times 1536	≈ 0	19.26T	12556	775
RAFT-Stereo [15]	11.1M	1536 \times 1536	4.42G	28.74T	11278	630
FoundationStereo [16]	375M	1536 \times 1536	4.42G	110.76T	30488 †	2469 †
MatchStereo-T	8.78M	1536 \times 1536 2176 \times 3840	16.5G 0.06T	0.34T 1.20T	2201(1492) 6030(3088)	93(38) 275(95)
MatchStereo-S	25.2M	1536 \times 1536 2176 \times 3840	0.03T 0.10T	0.98T 3.48T	2488(1774) 7294(4862)	131(45) 402(139)
MatchStereo-B	75.5M	1536 \times 1536 2176 \times 3840	0.05T 0.18T	3.59T 12.72T	4546(3010) 13680(8306)	239(75) 752(256)
MatchFlow-B	75.5M	1536 \times 1536 2176 \times 3840	0.05T 0.18T	3.60T 12.79T	4432(3298) 14344(10058)	236(77) 755(261)

TABLE 4

Ablation experiments. The baseline model is MatchDecoder-B. All model variants are trained for 100k steps with batch size 16 on the SceneFlow [14] dataset (L: Consistency-constrained loss, A: Attention weights as additional input of the projection layer, G: Gated cross-MatchAttention, N: Non-occlusion mask embedding in self-MatchAttention, Full: Baseline + L + A + G + N, LRI: Low resolution initialization applied to the full resolution ‘F’ dataset). Full + LRI are used as our final model for high-resolution images ($\geq 2K$).

Model Variants	Middlebury					
	F ($>2px$)		H ($>2px$)		Q ($>2px$)	
	All	Noc	All	Noc	All	Noc
Baseline	15.82	11.87	11.31	7.84	10.74	7.48
+ L	16.97	13.05	11.20	7.81	10.62	7.62
+ A	15.95	12.10	10.38	7.33	8.04	6.19
+ G	15.28	11.24	10.67	7.24	10.00	7.13
+ N	15.65	11.77	11.25	8.02	10.28	7.36
Full	14.80	11.04	9.23	6.24	8.16	5.45
Full + LRI	13.32	9.73	-	-	-	-
Full - L	15.60	11.80	9.58	6.28	8.89	5.94
Full - A	15.40	11.48	11.01	7.73	9.84	6.78
Full - G	15.24	11.18	10.86	7.56	9.96	6.79
Full - N	15.20	11.45	8.62	5.52	8.28	5.34
Full (dot product)	14.92	11.06	9.48	6.18	9.69	6.77

R'_{pos} , which is then downsampled to 1/32 of the original image resolution and used to replace the initial correlation for the full-resolution inference. The initial correlation may not scale well at high resolution and LRI can provide a more robust initial relative position. The Full + LRI configuration provides an additional 10% improvement at full resolution and is used for high-resolution images ($\geq 2K$).

Negative L1-Norm: Comparing Full vs Full (dot product) validates the negative L1-norm similarity measure, showing 0.8% improvement at full resolution, 2.6% at half resolution, and 15.8% at quarter resolution. The increasing benefits at lower resolutions confirm that L1-norm’s sparsity bias becomes more valuable when fewer fine-grained features are available for discrimination.

Cumulative Component Analysis: The full model (Baseline + L + A + G + N) achieves substantial improvements.

TABLE 5

Zero-shot generalization comparison of optical flow. ‘EPE’ metric is used for Sintel.

Methods	Sintel		KITTI	
	Clean	Final	EPE	Fl-all
PWC-Net [69]	2.55	3.93	10.4	33.7
RAFT [40]	1.43	2.71	5.04	17.4
GMA [70]	1.30	2.74	4.69	17.1
SKFlow [71]	1.22	2.46	4.27	15.5
FlowFormer [72]	<u>1.01</u>	<u>2.40</u>	4.09	14.7
DIP [73]	1.30	2.82	4.29	13.7
EMD-L [74]	0.88	2.55	4.12	13.5
CRAFT [75]	1.27	2.79	4.88	17.5
RPKNet [76]	1.12	2.45	-	13.0
GMFlowNet [77]	1.14	2.71	4.24	15.4
SEA-RAFT(M) [78]	1.21	4.04	4.29	14.2
SEA-RAFT(L) [78]	1.19	4.11	3.62	<u>12.9</u>
MatchFlow-B	1.17	2.28	<u>3.76</u>	10.9

The synergistic effect of all proposed components works together to eliminate the influence of occluded regions on the matching process. When any single component is removed from the full model, performance degradation occurs because the occlusion handling capability is compromised. Importantly, by eliminating the negative influence of occluded regions, the model can focus more effectively on learning accurate correspondences in non-occluded (Noc) regions, leading to improved overall performance.

5.4 Zero-shot Generalization

Zero-shot generalization enables practical deployment without domain-specific training data. We evaluate MatchAttention’s cross-domain transfer capabilities on stereo matching and optical flow tasks, training exclusively on synthetic Scene Flow [14] and testing on diverse real-world datasets.

Zero-Shot Optical Flow. Table 5 demonstrates MatchFlow-B’s competitive zero-shot generalization performance on optical flow estimation. MatchFlow-B achieves 2.28 EPE on Sintel Final pass [59] and 10.9% F1-All score on KITTI 2015 [18] dataset, outperforming all compared methods. Table 6 shows zero-shot generalization comparison of optical flow

TABLE 6

Zero-shot generalization comparison of optical flow on the high-resolution Spring dataset under ' $> 1\text{px}$ ' error metric. \dagger means out-of-memory at inference.

Methods	Spring train		Spring test
	2K	4K	2K
PWC-Net [69]	4.94	9.78	82.2
RAFT [40]	3.85	10.7	6.79
GMA [70]	3.75	\dagger	7.07
SKFlow [71]	3.79	\dagger	-
FlowFormer [72]	3.78	9.53	6.51
DIP [73]	3.64	9.53	-
GMFlow+ [79]	5.72	\dagger	-
RPKNet [76]	3.28	<u>7.35</u>	4.80
MemFlow [80]	<u>3.24</u>	\dagger	<u>5.76</u>
SEA-RAFT(M) [78]	3.47	8.22	-
MatchFlow-B	3.04	7.08	4.58

on the high-resolution Spring [19] dataset. MatchFlow-B consistently outperform the other methods including the recent RPKNet [76], MemFlow [80], and SEA-RAFT [78].

Zero-Shot Stereo Matching. Table 7 presents comprehensive zero-shot stereo matching results across multiple real-world datasets. On the challenging Middlebury dataset with high-resolution indoor scenarios and complex geometries, MatchStereo-B achieves 12.44% error at full resolution (F, All), significantly outperforming RAFT-Stereo (15.63%). The ETH3D results further validate effectiveness across mixed indoor and outdoor scenes, with MatchStereo-B achieving competitive 2.88% error.

MatchStereo-B* employs a fixed resolution inference (FRI) strategy, resizing all input images to 1536×1536 . This approach provides multiple benefits: (1) For high-resolution images like Middlebury 'F' dataset (2000×3000), it effectively reduces computational cost; (2) For lower-resolution images, it improves accuracy through upsampling; (3) Fixed resolution inference simplifies hardware optimization for practical deployment. MatchStereo-B* achieves superior results across all Middlebury resolutions: 12.37% (F, All), 8.43% (H, All), and 5.74% (Q, All), outperforming all the other methods. On ETH3D, MatchStereo-B* also achieves the lowest error.

We also evaluated FRI for RAFT-Stereo. The result of RAFT-Stereo* does not have the performance gain as that of MatchStereo-B*, highlighting the importance of architectural design for resolution adaptation.

Scale Ability Analysis. MatchAttention demonstrates excellent scaling properties across both data and model dimensions. Models trained on the large-scale FSD Mix dataset (1M+ images) achieve significantly higher accuracy than those trained on smaller Scene Flow (30K+ images), as evidenced by the results in Table 7. The improvements are particularly significant on the challenging Middlebury dataset: MatchStereo-B with FSD Mix training achieves 5.67% (F, All), 4.46% (H, All), and 4.58% (Q, All) compared to Scene Flow training's 12.44% (F, All), 8.97% (H, All), and 7.60% (Q, All). MatchStereo variants show consistent performance improvements with increased parameters from MatchStereo-T to MatchStereo-B, with each scale increase providing measurable accuracy gains across all evaluation datasets. This consistent scaling behavior validates the ar-

chitectural design's ability to effectively utilize additional computational resources.

Cross-Task Generalization. MatchFlow and MatchStereo share the same set of parameters and MatchFlow-B trained on Scene Flow optical flow data can perform stereo matching tasks. While there is a performance gap compared to stereo-specific training in Table 7, this demonstrates the architectural flexibility of MatchAttention and its ability to learn generalizable cross-view correspondence representations.

Architectural Benefits for Generalization. The superior zero-shot performance can be attributed to MatchAttention's key architectural advantages: (1) The explicit matching mechanism with learnable relative positions adapts naturally to varying disparity and flow ranges across different datasets; (2) The negative L1-norm similarity measure exploits the inherent sparsity of matching relationships, providing robustness to domain-specific appearance variations; (3) The linear complexity design maintains consistent performance across different image resolutions without architectural modifications. These properties collectively enable MatchAttention to maintain strong performance when transferring from synthetic training environments to diverse real-world scenarios.

5.5 Benchmark performance.

MatchStereo-B achieved the lowest average error (AvgErr) on the Middlebury benchmark at the time of algorithm submission, establishing new state-of-the-art performance. As demonstrated in Table 8, MatchStereo-B achieves 0.73 AvgErr, outperforming all comparative methods including FoundationStereo [16] (0.78 AvgErr).

The detailed benchmark performance on four real-world benchmarks, including KITTI 2012 Reflective [17], KITTI 2015 [18], ETH3D [13], and Middlebury [12], is summarized in Table 9. On the high-resolution Middlebury benchmark, MatchStereo-B outperforms all other methods except FoundationStereo for $> 2\text{px}$ metric (1.85 vs 1.84). The default $> 2\text{px}$ metric for Middlebury benchmark is a weighted average of $> 2\text{px}$ error of 15 test scenes with difficult scenes having weight 0.5 and other scenes weight 1. If we use mean average ($> 2\text{px}^\dagger$), MatchStereo-B clearly outperforms FoundationStereo (1.90 vs 2.02). For the sub-pixel $> 0.5\text{px}$ metric, MatchStereo-B outperforms all competing methods, demonstrating its capability to recover highly accurate depth.

On the ETH3D dataset, MatchStereo-B demonstrates robust second-tier performance across three evaluation metrics: 1.70% for $> 0.5\text{px}$, 0.70% for $> 1\text{px}$, and 0.11 for AvgErr. While maintaining competitive accuracy relative to FoundationStereo, MatchStereo-B demonstrates substantial computational advantages. As detailed in Table 3, MatchStereo-B requires only 3.59T FLOPs compared to FoundationStereo's 110.76T FLOPs at 1536×1536 resolution, representing a remarkable $30.8\times$ FLOPs reduction. The memory consumption achieves a $6.7\times$ reduction (4546MB vs 30488MB). Moreover, the disparities of both views can be estimated simultaneously for MatchStereo while FoundationStereo and DEFOM-Stereo can only estimate the disparity of the left view in a single run.

TABLE 7

Zero-shot stereo generalization and zero-shot flow to stereo transfer. Methods with * denote inference at a fixed 1536×1536 resolution.

Method	KITTI-15 >3px		F (>2px)		Middlebury H (>2px)		Q (>2px)		ETH3D >1px	
	All	Noc	All	Noc	All	Noc	All	Noc	All	Noc
Training Set			Scene Flow - Stereo Set							
DSMNet [81]	5.50	5.19	41.96	38.54	18.74	14.49	13.75	9.44	4.03	3.62
CFNet [82]	5.99	5.79	35.21	30.05	21.99	17.69	14.21	10.51	6.08	5.48
Graft-PSMNet [83]	5.34	5.00	39.92	36.30	17.65	13.36	13.92	9.23	11.43	10.7
ITSA-CFNet [84]	4.73	4.67	34.01	30.14	16.48	12.32	12.28	8.54	5.43	5.17
HVT-PSMNet [85]	4.84	4.63	40.74	37.60	15.66	12.55	10.12	7.00	6.07	5.65
RAFT-Stereo [15]	5.47	5.27	15.63	11.94	11.20	8.66	10.25	7.44	<u>2.60</u>	<u>2.29</u>
RAFT-Stereo* [15]	5.81	5.63	15.75	12.26	10.17	7.54	8.45	6.35	4.23	3.99
IGEV-Stereo [43]	6.03	5.76	30.94	28.98	11.90	9.45	8.88	6.20	4.04	3.60
NMRF-Stereo [86]	5.31	5.14	37.63	35.25	13.36	10.9	7.87	5.07	3.80	3.48
Mocha-Stereo [87]	5.97	5.73	30.23	28.26	10.18	9.45	7.96	<u>4.87</u>	4.02	3.47
MatchStereo-T	5.68	5.46	15.49	11.30	11.30	7.83	10.24	7.16	4.25	3.82
MatchStereo-S	5.65	5.46	13.45	9.88	10.06	6.81	8.98	5.92	3.62	3.24
MatchStereo-B	5.34	5.15	<u>12.44</u>	<u>9.13</u>	8.97	<u>6.23</u>	7.60	5.11	2.88	2.69
MatchStereo-B*	5.04	4.87	12.37	8.87	8.43	5.62	5.74	3.72	2.57	2.25
Training Set			Scene Flow - Flow Set							
MatchFlow-B	6.15	5.91	16.88	12.76	12.47	8.46	13.01	9.35	4.29	4.03
MatchFlow-B*	6.04	5.79	17.43	12.91	11.08	7.53	7.60	4.99	3.68	3.30
Training Set			FSD Mix							
MatchStereo-T	4.26	4.08	7.87	4.30	6.62	3.70	7.32	4.42	2.12	1.98
MatchStereo-S	3.90	3.74	6.59	3.54	5.22	2.75	5.15	3.16	1.91	1.81
MatchStereo-B	3.78	3.63	5.67	2.84	4.46	2.27	4.58	2.69	1.36	1.27
MatchStereo-B*	3.98	3.81	6.56	3.59	4.07	2.04	2.98	1.40	2.68	2.43

TABLE 8

Average error (EPE) on Middlebury test set. MatchStereo-B ranked first on the benchmark among all submission methods (2025-05-10).

avgerr (pixels)		Weight																	
Name	Res	Avg	Austr	AustrP	Bicyc2	Class	ClassE	Compu	Crusa	CrusaP	Djemb	DjembL	Hoops	Livgrm	Nkuba	Plants	Stairs		
MatchStereo (Ours)	F	0.73 1	1.43 16	1.27 11	0.53 2	0.57 7	0.73 2	0.53 4	0.72 4	0.80 19	0.32 10	0.51 6	0.67 1	0.54 5	1.07 3	0.90 3	0.49 2		
FoundationStereo [16]	F	0.78 3	1.45 18	1.37 18	0.69 33	0.55 2	1.14 18	0.48 1	0.66 1	0.63 1	0.31 7	0.42 2	0.83 2	0.63 9	1.24 11	1.00 6	0.52 3		
DEFOM-Stereo [67]	F	0.79 4	1.14 1	1.16 4	0.53 2	0.57 7	1.07 13	0.50 2	0.76 7	0.73 8	0.39 25	0.53 7	1.73 32	0.53 2	1.12 8	1.06 9	0.55 5		
AIO-Stereo [45]	F	0.85 7	1.37 10	1.26 10	0.60 14	0.58 10	1.23 25	0.54 5	1.05 25	0.76 14	0.30 3	0.58 12	1.41 17	0.70 17	1.07 3	1.12 11	0.66 7		
Selective-IGEV [44]	F	<u>0.91</u> 10	1.44 17	1.40 23	0.60 14	0.69 23	1.36 35	0.55 9	1.06 28	0.76 14	0.32 10	0.63 15	1.24 13	0.70 17	1.09 5	1.18 17	1.46 38		
StereoAnywhere [88]	F	<u>0.93</u> 13	1.50 23	1.06 1	0.60 14	0.96 45	2.77 80	0.59 17	0.82 9	0.75 13	0.39 25	0.70 22	1.00 5	0.53 2	1.71 33	0.98 5	0.59 6		

TABLE 9

Benchmark performance on four real-world datasets. All error metrics are reported from the public available benchmark sites. For the ETH3D and Middlebury datasets, the default 'Noc' mask is used. > 2px[†] means averaging the > 2px error of the 15 test scenes w/o difficulty weighting.

Methods	KITTI-12 Reflective		KITTI-15		ETH3D			Middlebury			
	>2px-Noc	>2px-All	D1-fg	D1-All	>0.5px	>1px	AvgErr	>0.5px	>2px	>2px [†]	AvgErr
GMStereo [79]	-	-	3.14	1.77	5.94	1.83	0.19	51.5	7.14	7.75	1.31
RAFT-Stereo [15]	-	-	-	-	7.04	2.44	0.18	27.7	4.74	5.23	1.27
CREStereo [60]	9.71	11.26	2.86	1.69	3.58	0.98	0.13	28.0	3.71	3.97	1.15
IGEV-Stereo [43]	7.57	8.80	2.67	1.59	3.52	1.12	0.14	32.4	4.83	4.77	2.89
MoCha-Stereo [87]	6.97	8.10	2.43	1.53	3.20	1.41	0.13	24.8	3.51	3.49	1.10
Selective-IGEV [44]	6.73	7.84	2.61	1.55	3.06	1.23	0.12	24.6	2.51	2.88	0.91
AIO-Stereo [45]	6.02	6.95	2.57	1.54	2.91	0.94	0.13	24.0	2.39	2.71	0.85
DEFOM-Stereo [67]	<u>5.76</u>	<u>6.72</u>	2.23	1.41	2.21	0.70	0.11	25.2	2.36	2.67	0.79
StereoAnywhere [88]	-	-	-	-	-	-	-	27.3	3.69	4.34	0.93
FoundationStereo [16]	-	-	-	-	1.26	0.26	0.09	<u>22.5</u>	1.84	<u>2.02</u>	<u>0.78</u>
MatchStereo-B (Ours)	5.53	6.64	<u>2.32</u>	<u>1.50</u>	<u>1.70</u>	<u>0.70</u>	<u>0.11</u>	21.8	<u>1.85</u>	1.90	0.73

On the KITTI 2015 benchmark, MatchStereo-B has secondary performance to DEFOM-Stereo [67]. On the challenging KITTI 2012 reflective benchmark, MatchStereo-B outperforms all other methods including DEFOM-Stereo. MatchStereo-B achieves 29ms inference time for KITTI resolution (384×1248) stereo pairs with FP16 precision and torch.compile enabled, demonstrating its practical viability for real-world deployment scenarios.

DEFOM-Stereo and Foundation Stereo both employ the pre-trained depth foundation model, Depth Anything V2 [48], to enhance the feature extraction capability of their encoders. In contrast, MatchStereo relies solely on a pure CNN encoder trained from scratch, yet still achieves competitive performance. It is worth noting that the strategy of augmenting the encoder with a depth foundation model is also compatible with MatchStereo. However, due to the high computational complexity and memory consumption of the ViT encoder at high resolutions (primarily caused by the quadratic complexity of global attention), this strategy has not been implemented for MatchStereo.

The comprehensive benchmark evaluation demonstrates MatchStereo has achieved state-of-the-art performance across multiple challenging datasets while maintaining superior computational efficiency.

6 CONCLUSION

This paper proposes MatchAttention, an attention mechanism that dynamically matches relative positions. MatchAttention possesses the advantages of long-range connection, explicit matching, and linear computational complexity, making it suitable for high-resolution cross-view matching.

The hierarchical cross-view decoder MatchDecoder, built with MatchAttention as its core component, can be applied to general cross-view matching tasks and has achieved state-of-the-art performance in stereo matching and optical flow. The proposed gated cross-MatchAttention and consistency-constrained loss demonstrate that removing the influence of occlusion in both forward and backward passes allows the model to focus on learning the matching relationships themselves, further improving performance. MatchStereo has significantly lower computational complexity (FLOPs) compared to algorithms with similar accuracy. MatchStereo-T can perform inference on 4K UHD images within 0.1 seconds, while MatchStereo-B can process KITTI-resolution images in 29ms, enabling real-time, high-resolution, and high-accuracy stereo inference.

Future work includes applying MatchDecoder to other cross-view matching tasks such as feed-forward 3D Gaussian splatting to make it suitable for even higher resolutions. On the other hand, given the strong data and parameter scalability of MatchStereo, we plan to train larger models on larger-scale datasets.

ACKNOWLEDGMENTS

REFERENCES

- [1] S. Wang, V. Leroy, Y. Cabon, B. Chidlovskii, and J. Revaud, "Dust3r: Geometric 3d vision made easy," in *IEEE Conf. Comput. Vis. Pattern Recog.*, June 2024, pp. 20 697–20 709.
- [2] Y. Chen, H. Xu, C. Zheng, B. Zhuang, M. Pollefeys, A. Geiger, T.-J. Cham, and J. Cai, "Mvsplat: Efficient 3d gaussian splatting from sparse multi-view images," *Eur. Conf. Comput. Vis.*, pp. 370–386, 2024.
- [3] B. Smart, C. Zheng, I. Laina, and V. A. Prisacariu, "Splatt3r: Zero-shot gaussian splatting from uncalibrated image pairs," *arXiv preprint arXiv:2408.13912*, 2024.
- [4] B. Ye, S. Liu, H. Xu, L. Xueting, M. Pollefeys, M.-H. Yang, and P. Songyou, "No pose, no problem: Surprisingly simple 3d gaussian splats from sparse unposed images," *arXiv preprint arXiv:2410.24207*, 2024.
- [5] H. Xu, J. Zhang, J. Cai, H. Rezatofighi, F. Yu, D. Tao, and A. Geiger, "Unifying flow, stereo and depth estimation," *IEEE Trans. Pattern Anal. Mach. Intell.*, vol. 45, no. 11, pp. 13 941–13 958, 2023.
- [6] V. Leroy, Y. Cabon, and J. Revaud, "Grounding image matching in 3d with mast3r," in *Eur. Conf. Comput. Vis.*, 2024, pp. 71–91.
- [7] J. Sun, Z. Shen, Y. Wang, H. Bao, and X. Zhou, "LoFTR: Detector-free local feature matching with transformers," in *IEEE Conf. Comput. Vis. Pattern Recog.*, June 2021, pp. 8922–8931.
- [8] K. He, X. Zhang, S. Ren, and J. Sun, "Deep residual learning for image recognition," in *IEEE Conf. Comput. Vis. Pattern Recog.*, June 2016.
- [9] K. Xu, J. L. Ba, R. Kiros, K. Cho, A. Courville, R. Salakhutdinov, R. S. Zemel, and Y. Bengio, "Show, attend and tell: neural image caption generation with visual attention," in *Int. Conf. Mach. Learn.*, 2015, p. 2048–2057.
- [10] T. Luong, H. Pham, and C. D. Manning, "Effective approaches to attention-based neural machine translation," in *Empirical Methods in Natural Language Processing, EMNLP*, 2015, pp. 1412–1421.
- [11] X. Zhu, W. Su, L. Lu, B. Li, X. Wang, and J. Dai, "Deformable detr: Deformable transformers for end-to-end object detection," in *Int. Conf. Learn. Represent.*, 2021.
- [12] D. Scharstein, H. Hirschmüller, Y. Kitajima, G. Krathwohl, N. Nešić, X. Wang, and P. Westling, "High-resolution stereo datasets with subpixel-accurate ground truth," in *Pattern Recog. German Conf.*, 2014, pp. 31–42.
- [13] T. Schops, J. L. Schonberger, S. Galliani, T. Sattler, K. Schindler, M. Pollefeys, and A. Geiger, "A multi-view stereo benchmark with high-resolution images and multi-camera videos," in *IEEE Conf. Comput. Vis. Pattern Recog.*, 2017, pp. 3260–3269.
- [14] N. Mayer, E. Ilg, P. Hausser, P. Fischer, D. Cremers, A. Dosovitskiy, and T. Brox, "A large dataset to train convolutional networks for disparity, optical flow, and scene flow estimation," in *IEEE Conf. Comput. Vis. Pattern Recog.*, 2016, pp. 4040–4048.
- [15] L. Lipson, Z. Teed, and J. Deng, "Raft-stereo: Multilevel recurrent field transforms for stereo matching," in *Int. Conf. 3D Vision*, 2021, pp. 218–227.
- [16] B. Wen, M. Trepte, J. Aribido, J. Kautz, O. Gallo, and S. Birchfield, "Foundationstereo: Zero-shot stereo matching," in *IEEE Conf. Comput. Vis. Pattern Recog.*, June 2025, pp. 5249–5260.
- [17] A. Geiger, P. Lenz, and R. Urtasun, "Are we ready for autonomous driving? the kitti vision benchmark suite," in *IEEE Conf. Comput. Vis. Pattern Recog.*, 2012.
- [18] M. Menze, C. Heipke, and A. Geiger, "Joint 3d estimation of vehicles and scene flow," *ISPRS Ann. Photogrammetry, Remote Sens. Spatial Inf. Sciences*, vol. 2, p. 427, 2015.
- [19] L. Mehl, J. Schmalfluss, A. Jahedi, Y. Nalivayko, and A. Bruhn, "Spring: A high-resolution high-detail dataset and benchmark for scene flow, optical flow and stereo," in *IEEE Conf. Comput. Vis. Pattern Recog.*, June 2023, pp. 4981–4991.
- [20] D. Bahdanau, K. Cho, and Y. Bengio, "Neural machine translation by jointly learning to align and translate," in *Int. Conf. Learn. Represent.*, 2015.
- [21] D. Han, Y. Pu, Z. Xia, Y. Han, X. Pan, X. Li, J. Lu, S. Song, and G. Huang, "Bridging the divide: Reconsidering softmax and linear attention," in *Adv. Neural Inform. Process. Syst.*, vol. 37, 2024, pp. 79 221–79 245.
- [22] I. Beltagy, M. E. Peters, and A. Cohan, "Longformer: The long-document transformer," *arXiv:2004.05150*, 2020.
- [23] M. Zaheer, G. Guruganesh, K. A. Dubey, J. Ainslie, C. Albeti, S. Ontanon, P. Pham, A. Ravula, Q. Wang, L. Yang *et al.*, "Big bird: Transformers for longer sequences," *Adv. Neural Inform. Process. Syst.*, vol. 33, 2020.
- [24] C. Lou, Z. Jia, Z. Zheng, and K. Tu, "Sparsers is faster and less is more: Efficient sparse attention for long-range transformers," *arXiv:2406.16747*, 2024.

- [25] A. Hassani, S. Walton, J. Li, S. Li, and H. Shi, "Neighborhood attention transformer," in *IEEE Conf. Comput. Vis. Pattern Recog.*, June 2023, pp. 6185–6194.
- [26] S. Liu, Z. Tan, and X. Wang, "Clear: Conv-like linearization revs pre-trained diffusion transformers up," *arXiv preprint arXiv:2412.16112*, 2024.
- [27] Z. Liu, Y. Lin, Y. Cao, H. Hu, Y. Wei, Z. Zhang, S. Lin, and B. Guo, "Swin transformer: Hierarchical vision transformer using shifted windows," in *Int. Conf. Comput. Vis.*, October 2021, pp. 10012–10022.
- [28] Z. Li, W. Wang, H. Li, E. Xie, C. Sima, T. Lu, Y. Qiao, and J. Dai, "Bevformer: Learning bird's-eye-view representation from multi-camera images via spatiotemporal transformers," in *Eur. Conf. Comput. Vis.*, 2022, pp. 1–18.
- [29] A. Vaswani, N. Shazeer, N. Parmar, J. Uszkoreit, L. Jones, A. N. Gomez, L. u. Kaiser, and I. Polosukhin, "Attention is all you need," in *Adv. Neural Inform. Process. Syst.*, vol. 30, 2017.
- [30] Z. Liu, H. Hu, Y. Lin, Z. Yao, Z. Xie, Y. Wei, J. Ning, Y. Cao, Z. Zhang, L. Dong, F. Wei, and B. Guo, "Swin transformer v2: Scaling up capacity and resolution," in *IEEE Conf. Comput. Vis. Pattern Recog.*, June 2022, pp. 12 009–12 019.
- [31] D. Shi, "Transnext: Robust foveal visual perception for vision transformers," in *IEEE Conf. Comput. Vis. Pattern Recog.*, June 2024, pp. 17 773–17 783.
- [32] J. Su, M. Ahmed, Y. Lu, S. Pan, W. Bo, and Y. Liu, "Roformer: Enhanced transformer with rotary position embedding," *Neuro-comput.*, vol. 568, no. C, February 2024.
- [33] A. Grattafiori, A. Dubey, A. Jauhri, A. Pandey, A. Kadian, A. Al-Dahle, A. Letman, A. Mathur, A. Schelten, A. Vaughan, A. Yang, A. Fan, and et al., "The llama 3 herd of models," *arXiv:2407.21783*, 2024.
- [34] P. Weinzaepfel, T. Lucas, V. Leroy, Y. Cabon, V. Arora, R. Brégier, G. Csurka, L. Antsfeld, B. Chidlovskii, and J. Revaud, "Croco v2: Improved cross-view completion pre-training for stereo matching and optical flow," in *Int. Conf. Comput. Vis.*, 2023, pp. 17 969–17 980.
- [35] R. Li, B. Yi, J. Liu, H. Gao, Y. Ma, and A. Kanazawa, "Cameras as relative positional encoding," *arXiv:2507.10496*, 2025.
- [36] Z. Li, X. Liu, N. Drenkow, A. Ding, F. X. Creighton, R. H. Taylor, and M. Unberath, "Revisiting stereo depth estimation from a sequence-to-sequence perspective with transformers," in *Int. Conf. Comput. Vis.*, 2021, pp. 6197–6206.
- [37] A. Kendall, H. Martirosyan, S. Dasgupta, P. Henry, R. Kennedy, A. Bachrach, and A. Bry, "End-to-end learning of geometry and context for deep stereo regression," in *Int. Conf. Comput. Vis.*, 2017, pp. 66–75.
- [38] J.-R. Chang and Y.-S. Chen, "Pyramid stereo matching network," in *IEEE Conf. Comput. Vis. Pattern Recog.*, 2018, pp. 5410–5418.
- [39] A. Bangunharcana, J. W. Cho, S. Lee, I. S. Kweon, K.-S. Kim, and S. Kim, "Correlate-and-excite: Real-time stereo matching via guided cost volume excitation," in *Int. Conf. Intell. Robots Syst.*, 2021.
- [40] Z. Teed and J. Deng, "Raft: Recurrent all-pairs field transforms for optical flow," in *Eur. Conf. Comput. Vis.* Springer, 2020, pp. 402–419.
- [41] T. Tanai, Y. Matsushita, Y. Sato, and T. Naemura, "Continuous 3D Label Stereo Matching using Local Expansion Moves," *IEEE Trans. Pattern Anal. Mach. Intell.*, vol. 40, no. 11, pp. 2725–2739, 2018.
- [42] T. Yan, X. Yang, G. Yang, and Q. Zhao, "Hierarchical belief propagation on image segmentation pyramid," *IEEE Trans. Image Process.*, vol. 32, pp. 4432–4442, 2023.
- [43] G. Xu, X. Wang, X. Ding, and X. Yang, "Iterative geometry encoding volume for stereo matching," in *IEEE Conf. Comput. Vis. Pattern Recog.*, 2023, pp. 21 919–21 928.
- [44] X. Wang, G. Xu, H. Jia, and X. Yang, "Selective-stereo: Adaptive frequency information selection for stereo matching," in *IEEE Conf. Comput. Vis. Pattern Recog.*, 2024, pp. 19 701–19 710.
- [45] J. Zhou, H. Zhang, J. Yuan, P. Ye, T. Chen, H. Jiang, M. Chen, and Y. Zhang, "All-in-one: Transferring vision foundation models into stereo matching," in *Assoc. Advancement Artif. Intell.*, February 2025.
- [46] M. Oquab, T. Darcet, T. Moutakanni, H. V. Vo, M. Szafraniec, V. Khalidov, P. Fernandez, D. HAZIZA, F. Massa, A. El-Nouby, M. Assran, N. Ballas, W. Galuba, R. Howes, P.-Y. Huang, S.-W. Li, I. Misra, M. Rabbat, V. Sharma, G. Synnaeve, H. Xu, H. Jegou, J. Mairal, P. Labatut, A. Joulin, and P. Bojanowski, "DINOv2: Learning robust visual features without supervision," *Transactions on Machine Learning Research*, 2024.
- [47] A. Kirillov, E. Mintun, N. Ravi, H. Mao, C. Rolland, L. Gustafson, T. Xiao, S. Whitehead, A. C. Berg, W.-Y. Lo, P. Dollar, and R. Girshick, "Segment anything," in *Int. Conf. Comput. Vis.*, October 2023, pp. 4015–4026.
- [48] L. Yang, B. Kang, Z. Huang, Z. Zhao, X. Xu, J. Feng, and H. Zhao, "Depth anything v2," in *Adv. Neural Inform. Process. Syst.*, 2024.
- [49] R. Ranftl, A. Bochkovskiy, and V. Koltun, "Vision transformers for dense prediction," in *Int. Conf. Comput. Vis.*, October 2021, pp. 12 179–12 188.
- [50] A. Dosovitskiy, L. Beyer, A. Kolesnikov, D. Weissenborn, X. Zhai, T. Unterthiner, M. Dehghani, M. Minderer, G. Heigold, S. Gelly et al., "An image is worth 16x16 words: Transformers for image recognition at scale," in *Int. Conf. Learn. Represent.*, 2020.
- [51] D. A. Tarzanagh, Y. Li, C. Thrampoulidis, and S. Oymak, "Transformers as support vector machines," in *Adv. Neural Inform. Process. Syst.*, 2023.
- [52] W. Yu, C. Si, P. Zhou, M. Luo, Y. Zhou, J. Feng, S. Yan, and X. Wang, "Metaformer baselines for vision," *IEEE Trans. Pattern Anal. Mach. Intell.*, vol. 46, no. 2, pp. 896–912, 2024.
- [53] D. Hendrycks and K. Gimpel, "Gaussian error linear units (GELUs)," *arXiv:1606.08415*, 2023.
- [54] O. Ronneberger, P. Fischer, and T. Brox, "U-net: Convolutional networks for biomedical image segmentation," 2015, pp. 234–241.
- [55] X. Chu, Z. Tian, B. Zhang, X. Wang, and C. Shen, "Conditional positional encodings for vision transformers," in *Int. Conf. Learn. Represent.*, 2023.
- [56] S. Elfving, E. Uchibe, and K. Doya, "Sigmoid-weighted linear units for neural network function approximation in reinforcement learning," *Neural Netw.*, vol. 107, pp. 3–11, 2018.
- [57] P. Xu, Z. Xiang, C. Qiao, J. Fu, and X. Zhao, "Adaptive multi-modal cross-entropy loss for stereo matching," in *IEEE Conf. Comput. Vis. Pattern Recog.*, 2024.
- [58] I. Loshchilov and F. Hutter, "Decoupled weight decay regularization," in *Int. Conf. Learn. Represent.*, 2019.
- [59] D. J. Butler, J. Wulff, G. B. Stanley, and M. J. Black, "A naturalistic open source movie for optical flow evaluation," in *Eur. Conf. Comput. Vis.* Springer, 2012, pp. 611–625.
- [60] J. Li, P. Wang, P. Xiong, T. Cai, Z. Yan, L. Yang, J. Liu, H. Fan, and S. Liu, "Practical stereo matching via cascaded recurrent network with adaptive correlation," in *IEEE Conf. Comput. Vis. Pattern Recog.*, 2022, pp. 16 263–16 272.
- [61] J. Tremblay, T. To, and S. Birchfield, "Falling things: A synthetic dataset for 3d object detection and pose estimation," in *IEEE Conf. Comput. Vis. Pattern Recog.*, 2018, pp. 2038–2041.
- [62] W. Bao, W. Wang, Y. Xu, Y. Guo, S. Hong, and X. Zhang, "In-stereo2k: a large real dataset for stereo matching in indoor scenes," *Sci. China Inf. Sci.*, vol. 63, pp. 1–11, 2020.
- [63] G. Yang, J. Manela, M. Happold, and D. Ramanan, "Hierarchical deep stereo matching on high-resolution images," in *IEEE Conf. Comput. Vis. Pattern Recog.*, 2019, pp. 5515–5524.
- [64] Y. Cabon, N. Murray, and M. Humenberger, "Virtual kitti 2," *arXiv:2001.10773*, 2020.
- [65] A. Dosovitskiy, P. Fischer, E. Ilg, P. Häusser, C. Hazırbaş, V. Golkov, P. v. d. Smagt, D. Cremers, and T. Brox, "Flownet: Learning optical flow with convolutional networks," in *Int. Conf. Comput. Vis.*, 2015, pp. 2758–2766.
- [66] D. Kondermann, R. Nair, K. Honauer, K. Krispin, J. Andrusis, A. Brock, B. Güssefeld, M. Rahimimoghaddam, S. Hofmann, C. Brenner, and B. Jähne, "The hci benchmark suite: Stereo and flow ground truth with uncertainties for urban autonomous driving," in *IEEE Conf. Comput. Vis. Pattern Recog. Worksh.*, 2016, pp. 19–28.
- [67] H. Jiang, Z. Lou, L. Ding, R. Xu, M. Tan, W. Jiang, and R. Huang, "Defom-stereo: Depth foundation model based stereo matching," in *IEEE Conf. Comput. Vis. Pattern Recog.*, June 2025, pp. 21 857–21 867.
- [68] A. Bochkovskiy, A. Delaunoy, H. Germain, M. Santos, Y. Zhou, S. R. Richter, and V. Koltun, "Depth pro: Sharp monocular metric depth in less than a second," in *Int. Conf. Learn. Represent.*, April 2025.
- [69] D. Sun, X. Yang, M.-Y. Liu, and J. Kautz, "Pwc-net: Cnns for optical flow using pyramid, warping, and cost volume," in *IEEE Conf. Comput. Vis. Pattern Recog.*, 2018, pp. 8934–8943.
- [70] S. Jiang, D. Campbell, Y. Lu, H. Li, and R. Hartley, "Learning to estimate hidden motions with global motion aggregation," in *Int. Conf. Comput. Vis.*, October 2021, pp. 9772–9781.

- [71] S. Sun, Y. Chen, Y. Zhu, G. Guo, and G. Li, "Skflow: Learning optical flow with super kernels," *Adv. Neural Inform. Process. Syst.*, vol. 35, pp. 11 313–11 326, 2022.
- [72] Z. Huang, X. Shi, C. Zhang, Q. Wang, K. C. Cheung, H. Qin, J. Dai, and H. Li, "Flowformer: A transformer architecture for optical flow," in *Eur. Conf. Comput. Vis.* Springer, 2022, pp. 668–685.
- [73] Z. Zheng, N. Nie, Z. Ling, P. Xiong, J. Liu, H. Wang, and J. Li, "Dip: Deep inverse patchmatch for high-resolution optical flow," in *IEEE Conf. Comput. Vis. Pattern Recog.*, 2022, pp. 8925–8934.
- [74] C. Deng, A. Luo, H. Huang, S. Ma, J. Liu, and S. Liu, "Explicit motion disentangling for efficient optical flow estimation," in *Int. Conf. Comput. Vis.*, 2023, pp. 9521–9530.
- [75] X. Sui, S. Li, X. Geng, Y. Wu, X. Xu, Y. Liu, R. Goh, and H. Zhu, "Craft: Cross-attentional flow transformer for robust optical flow," in *IEEE Conf. Comput. Vis. Pattern Recog.*, 2022, pp. 17 602–17 611.
- [76] H. Morimitsu, X. Zhu, X. Ji, and X.-C. Yin, "Recurrent partial kernel network for efficient optical flow estimation," *Assoc. Advancement Artif. Intell.*, vol. 38, no. 5, pp. 4278–4286, March 2024.
- [77] S. Zhao, L. Zhao, Z. Zhang, E. Zhou, and D. Metaxas, "Global matching with overlapping attention for optical flow estimation," in *IEEE Conf. Comput. Vis. Pattern Recog.*, 2022, pp. 17 592–17 601.
- [78] Y. Wang, L. Lipson, and J. Deng, "Sea-raft: Simple, efficient, accurate raft for optical flow," in *Eur. Conf. Comput. Vis.*, 2024, pp. 36–54.
- [79] H. Xu, J. Zhang, J. Cai, H. Rezatofighi, F. Yu, D. Tao, and A. Geiger, "Unifying flow, stereo and depth estimation," *IEEE Trans. Pattern Anal. Mach. Intell.*, 2023.
- [80] Q. Dong and Y. Fu, "Memflow: Optical flow estimation and prediction with memory," in *IEEE Conf. Comput. Vis. Pattern Recog.*, June 2024, pp. 19 068–19 078.
- [81] F. Zhang, X. Qi, R. Yang, V. Prisacariu, B. Wah, and P. Torr, "Domain-invariant stereo matching networks," in *Eur. Conf. Comput. Vis.* Springer, 2020, pp. 420–439.
- [82] Z. Shen, Y. Dai, and Z. Rao, "Cfnet: Cascade and fused cost volume for robust stereo matching," in *IEEE Conf. Comput. Vis. Pattern Recog.*, 2021, pp. 13 906–13 915.
- [83] B. Liu, H. Yu, and G. Qi, "Graftnet: Towards domain generalized stereo matching with a broad-spectrum and task-oriented feature," in *IEEE Conf. Comput. Vis. Pattern Recog.*, June 2022, pp. 13 012–13 021.
- [84] W. Chuah, R. Tennakoon, R. Hoseinnezhad, A. Bab-Hadiashar, and D. Suter, "Itsa: An information-theoretic approach to automatic shortcut avoidance and domain generalization in stereo matching networks," in *IEEE Conf. Comput. Vis. Pattern Recog.*, June 2022, pp. 13 022–13 032.
- [85] T. Chang, X. Yang, T. Zhang, and M. Wang, "Domain generalized stereo matching via hierarchical visual transformation," in *IEEE Conf. Comput. Vis. Pattern Recog.*, June 2023, pp. 9559–9568.
- [86] T. Guan, C. Wang, and Y.-H. Liu, "Neural markov random field for stereo matching," in *IEEE Conf. Comput. Vis. Pattern Recog.*, June 2024, pp. 5459–5469.
- [87] Z. Chen, W. Long, H. Yao, Y. Zhang, B. Wang, Y. Qin, and J. Wu, "Mocha-stereo: Motif channel attention network for stereo matching," in *IEEE Conf. Comput. Vis. Pattern Recog.*, 2024.
- [88] L. Bartolomei, F. Tosi, M. Poggi, and S. Mattoccia, "Stereo anywhere: Robust zero-shot deep stereo matching even where either stereo or mono fail," in *IEEE Conf. Comput. Vis. Pattern Recog.*, June 2025, pp. 1013–1027.



Tingman Yan received the B.S. degree from Beihang University, Beijing, China, in 2016, and the Ph.D. degree in control science and engineering from Shanghai Jiao Tong University, Shanghai, China. He is currently an Assistant Professor with the School of Control Science and Engineering, Dalian University of Technology. His research interests include stereo matching and 3D reconstruction.



an Associate Editor for IEEE Transactions on Industrial Informatics and as an Editorial Board Member for the International Journal of Control.



Xilian Yang received the B.S. and M.S. degrees from Beihang University, Beijing, China, in 2016 and 2019, respectively, and the Ph.D. degree in control science and engineering from Shanghai Jiao Tong University, Shanghai, China. She is currently an Assistant Professor with the School of Control Science and Engineering, Dalian University of Technology. Her research interests include stereo matching and machine learning.



Qunfei Zhao received the B.S.E.E. degree from Xi'an Jiao Tong University, Xi'an, China, in 1982, and the D.Sc. degree in system science from the Tokyo Institute of Technology, Tokyo, Japan, in 1988. He is a Professor at the School of Electronic Information and Electrical Engineering, Shanghai Jiao Tong University, China. His research interests include robotics, machine vision, and optimal control of complex mechatronic systems.



Zeyang Xia received the B.S. degree from Shanghai Jiao Tong University, Shanghai, China, in 2002, and the Ph.D. degree from Tsinghua University, Beijing, China, in 2008, both in mechanical engineering. He is currently a tenured Full Professor with the School of Mechanical Engineering, Shanghai Jiao Tong University. Previously, he served as a CAS Distinguished Professor and tenured Full Professor with Shenzhen Institutes of Advanced Technology, Chinese Academy of Sciences, Shenzhen, China.

He has served as an editorial board members for IEEE/ASME Transactions on Mechatronics, Robot, SmartBot, and as the General Chair of IEEE RCAR 2019. He is a Senior Member of IEEE/CIE/CAA, a Distinguished Member of CCF, and a Fellow of IET. Dr. Xia's research interests include robotics and biomechanics, with a focus on medical robotics, soft robotics, humanoid robotics, and computational biomechanics.